Spectrally Tunable Infrared Plasmonic $F,Sn:In_2O_3$ Nanocrystal Cubes

Shin Hum Cho †, Kevin M. Roccapriore //, Chandriker Kavir Dass §, Sandeep Ghosh †, Junho Choi ‡, Jungchul Noh †, Lauren Reimnitz †, Sungyeon Heo †, Kihoon Kim †, Karen Xie †, Brian A. Korgel †, Xiaoqin Li ‡, Joshua R. Hendrickson §, Jordan A. Hachtel //, Delia J. Milliron †

† McKetta Department of Chemical Engineering, The University of Texas at Austin, Austin, Texas 78712, United States
// Center for Nanophase Materials Science, Oak Ridge National Laboratory, Oak Ridge, Tennessee 37831, United States
§ Sensors Directorate, Air Force Research Laboratory, Wright-Patterson AFB, Ohio 45433, United States
‡ Department of Physics, Center for Complex Quantum Systems, The University of Texas, Austin, Texas 78712, United States

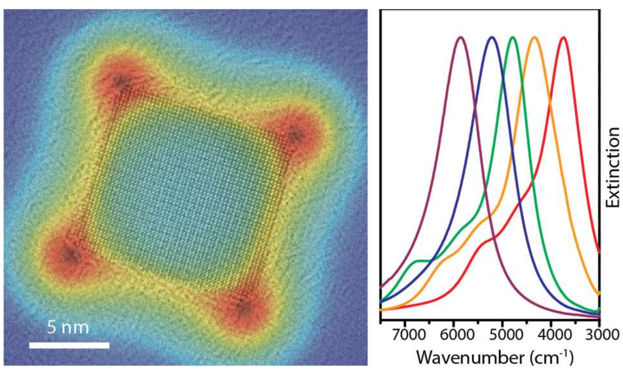

Abstract

A synthetic challenge in faceted metal oxide nanocrystals (NCs) is realizing tunable localized surface plasmon resonance (LSPR) near-field response in the infrared (IR). Cube-shaped nanoparticles of noble metal exhibit LSPR spectral tunability limited to visible spectral range. Here, we describe the colloidal synthesis of fluorine, tin co-doped indium oxide ($F,Sn:In_2O_3$) NC cubes with tunable IR range LSPR at 10 nm particle size range. Free carrier concentration in NC is tuned through controlled Sn dopant incorporation, where Sn is an aliovalent n-type dopant in In_2O_3 lattice. F shapes NC morphology into cubes by functioning as a surfactant on the {100} crystallographic facets. Cube shaped $F,Sn:In_2O_3$ NCs exhibit narrow, shape-dependent multimodal LSPR confined at corner, edge, and face centered modes. Monolayer NC array is fabricated through liquid-air phase assembly, further demonstrating tunable LSPR near-field enhancement (NFE) response as a NC film nanocavity. Tunable $F,Sn:In_2O_3$ NC near-field is coupled with PbS quantum dot, via Purcell effect. Detuning frequency between nanocavity and exciton is crafted, resulting in IR near-field dependent enhanced exciton lifetime decay. LSPR near-field tunability is directly visualized through IR range scanning transmission electron microscopy - electron energy loss spectroscopy (STEM-EELS). STEM-EELS mapping of spatially confined near-field at $F,Sn:In_2O_3$ NC array interparticle gap demonstrate NFE tunability.

Introduction

Colloidal synthesis of doped metal oxide nanocrystals (NCs) have emerged recently as a route for expanding localized surface plasmon resonance (LSPR) towards the infrared (IR) range.[1] With a suitable metal oxide NC host material, free electron compensating point defects are engineered by introducing additional n-type dopants. Doping strategies in plasmonic metal oxide NCs involve aliovalent cation substitution (e.g., $Sn:In_2O_3$,[2] Al:ZnO,[3] and In:CdO[4] NCs), and anionic fluorine dopant has been effectively incorporated (e.g., F,In:CdO,[5] $F,Sn:In_2O_3$,[6] and $F:In_2O_3$ NCs[7]) in metal oxide NC host lattice. Spectral advantages are nascent in doped metal oxide NC systems. Metal nanoparticles intrinsically possess high free-carrier concentrations exceeding 10^{23} cm^{-3}, leading to LSPR optical response restricted to the visible region of the electromagnetic spectrum.[8,9] Spectral tunability rely on increasing particle size in such metal classes of NCs to red-shift LSPR modes,[10,11] adding dimensional constraint in nano-assembly architecture. Alternatively, doped metal oxide NCs relieve particle size dependent constraint, expanding tunable IR range LSPR through controlled dopant incorporation with free-carrier concentration control in 10^{21} cm^{-3} range.[12,13] Intraband and interband transition effects optically observed in Au nanoparticles,[14] can be circumvented in doped metal oxide NCs. Due to low free-carrier concentration, LSPR mode located in the IR range are spaced apart from the UV range optical band edge in wide-bandgap metal oxide materials.[1,15]

Shape-dependent optical properties need be further developed in doped metal oxide classes of NCs to achieve spectral dominance in the IR. Colloidal Au and Ag cube nanoparticles sculpted by faceting agents lead to the observation of shape-dependent LSPR and enhanced electromagnetic near-fields at morphological discontinuities.[16,17] Halogen anions are capping agents that has been used for shape control of metal[18] and metal chalcogenide[19,20] classes of NCs, while shape control in LSPR active metal oxide[21] NCs are only recently being realized.[22] Morphologies reported for colloidal Au and Ag nanoparticle include cubes,[16,23,24] where faceted nanoparticles provide shape-dependent LSPR properties not observed in spherical particles. This including strong near-field enhancement (NFE) hot spots around corners and edges[17,25] that, in well-established metal nanoparticles, have been leveraged for plasmonic nanoantenna[26] and surface-enhanced Raman spectroscopy (SERS).[27,28] [18] Despite well-defined studies in noble metal NCs, limitations in IR range tunability for noble metal NCs are inherent. This included fixed high free carrier concentration, intraband or interband losses contributing to spectral linewidth, and spectral tunability dependent on particle size. Spectral tunability, while retaining high NFE will need be addressed through alternative materials for IR spectral dominance.

We advance LSPR spectral tunability in the IR range while preserving highly-faceted cube morphology, via co-doped $F,Sn:In_2O_3$ NCs. In our previous work, shape control in this recent class of nanocrystalline materials has been investigated using fluorine n-type dopant as a faceting agent in fluorine-doped indium oxide ($F:In_2O_3$) cube NCs, yet LSPR tuning was not realized.[7] Combining recent synthetic development employing a continuous slow injection of indium and dopant precursors into a heated reaction solution, high degree of NC shape and size control is realized.[29,30] The resulting LSPR properties with Sn and F co-dopants along with faceting effects are investigated. We show cationic Sn dopant is simultaneously incorporated into F surface passivated cube shaped In_2O_3 NCs to spectrally tune LSPR. Anionic F dopant suppress divalent scattering centers, leading to enhanced quality factor and narrow LSPR spectral linewidth. Controlled Sn dopant in NCs allows tunable carrier concentrations around 10^{21} cm^{-3}, resulting in synthetic access to IR range LSPR tunability control with high quality factor in NC solution dispersion.

Attaining advantages in IR range LSPR tunability, F,Sn:In_2O_3 NC solution dispersions are further self-assembled to fabricate dense plasmonic NC array film. Reliving spatial restrictions from size dependent LSPR tuning in prior noble metal nanoparticles, LSPR tunable F,Sn:In_2O_3 NCs allow densely packed nanogap cavities in monolayer film assembly area while retaining particle size. Spectrally tuned dense nanocavity array demonstrating NFE can be used to influence optical properties of alternate classes of nanocrystals. Utilizing strides in synthetic chemistry, access to two classes of photophysical light-matter interaction realm has been achieved over the past decade through colloidal nanocrystal synthesis.[31] Excitonic light emission of quantum dot (QD) is possible through quantum confinement effect, allowing photoluminescence in inorganic semiconductor bandgap materials (CdSe[32], InP[33], PbS[34], HgS[35]) through exciton electron-hole pair recombination. Meanwhile, confinement of electromagnetic field beyond the diffraction limit has been enabled through free-electron carrier confining nanoparticles smaller than λ/5 incident wavelength dimension, allowing LSPR induced NFE to occur.[36] Such maturation in two classes of nanocrystals allow hierarchical assembly of matter to be achieved. This was fabricated by stacking PbS QD and F,Sn:In_2O_3 NC monolayer films together through modified liquid-air phase self-assembly method.[37,38] Local and long-range NC ordering was respectively observed through SEM and SAXS, ensuring film uniformity. Self-assembled LSPR tunable F,Sn:In_2O_3 NCs allow degree of control in nanocavity film NFE detuning frequency to enhance PbS quantum dot lifetime decay rate at PL wavelength located at conventional-band (C-band) low-loss optical telecommunication window.[39,40] Excitonic and plasmonic light-matter interaction can optically be coupled when spatially in vicinity of each other, via Purcell effect. Strong LSPR near-field antenna NFE enhance photoluminescence (PL) lifetime decay rate in excitonic materials at the Purcell weak-coupling regime.[26,41] IR range LSPR near-field of F,Sn:In_2O_3 NC film array is observed to influence exciton decay rate in excitonic PbS QDs through optical time resolved PL measurement.

Such IR range LSPR near-field, expected to be spatially localized around F,Sn:In_2O_3 NCs, is directly visualized through monochromated scanning transmission electron microscopy - electron energy loss spectroscopy (STEM-EELS) technique.[42] With recent improvement in monochromator energy resolution,[43–45] STEM-EELS allow access to plasmonic near-field mapping under increasingly low-energy scales at nanoscale spatial resolution. Intense IR near-field spatially confined between F,Sn:In_2O_3 NC interparticle gap was directly visualized through EELS mapping. We observe that the F,Sn:In_2O_3 NC ordered array has emergent collective near-field ensemble behavior, unique from localized in-gap confined near-field mode. The collective NC film array ensemble was observed to have long range spatially delocalized near-field decay length at NC array edge. This was further supported by a delocalized volume mode extracted from Purcell enhancement PL decay lifetime in PbS coupled F,Sn:In_2O_3 NC film. The observed materials and optical characteristics lead to IR light near-field localization, making F,Sn:In_2O_3 NCs a gateway material in emergent IR near-field enhancement applications.

Experimental Methods

Materials: Indium (III) acetate (In(ac)$_3$, 99.99%), Tin (IV) acetate (Sn(ac)$_4$), Lead (II) chloride ($PbCl_2$, 99.999%), Sulfur (S, 99.99%), Oleic acid (OA, 90%, technical grade), Oleyl alcohol (OlAl, 85%, technical grade), Octane (98%, reagent grade), 1-Butanol (99.9%), Ethylene glycol (99.8%), and Tetrachloroethylene (99%, anhydrous) were purchased from Sigma-Aldrich. Tin (IV) fluoride (SnF_4, 99%) was purchased from Alfa Aesar. Oleylamine (OlAm, 80-90%) was purchased from Acros Organics. Hexane (99.9%), Acetone (99.5%, Certified ACS), Isopropyl alcohol (99.5%, Certified ACS), and Methanol (99.8%, Certified ACS) was purchased from Fisher Chemical. Hellmanex-III cleaning solution was purchased from Hellma Analytics. All chemicals were used as received without any further purification.

Fluorine Doped Indium Tin Oxide (F,Sn:In_2O_3) Cube Synthesis: All synthesis procedures are undertaken by employing standard Schlenk line techniques with modifications in continuous slow injection indium oxide NC synthesis.[29,46] In(acac)$_3$ 1342.97 mg (4.6 mmol), SnF_4 48.68 mg (5%, 0.25 mmol), Sn(ac)$_4$ 53.23 mg (3%, 0.15 mol), and oleic acid (10 ml) are loaded in a three-neck round-bottom flask in N_2 glove box. Precursor is stirred with magnetic bar at 600 rpm and degassed under vacuum at 120 °C for 15 mins, transferred to Schlenk line. Injection solution is added at rate of 0.2 ml/min, into 13 ml hot solution of oleyl alcohol maintained at 290 °C vented with 19-gauge needle under inert N_2 gas flow. Reaction mixture turns blue upon few minutes into injection. Subsequently, growth is terminated by removal of the heating mantle and cooled by blowing air on three-neck flask vessel. The nanocrystals are dispersed with hexane, then ethanol antisolvent was added and centrifuged at 7500 rpm for 10 mins. Washing procedure was repeated 3 times and nanocrystals are re-dispersed in 10 ml hexane. Resultant nanocrystal was centrifuged at 2000 rpm for 3 mins to remove non-dispersible aggregates and supernatant was collected for NC stock sample. Larger sized NCs were synthesized by controlling volume of injection solution (1 to 20 ml) while keeping other reaction parameters identical. Additional doped F,Sn:In_2O_3 NC (0 - 15 % Sn(ac)$_4$) concentration series are synthesized by controlling Sn(ac)$_4$ to In(ac)$_3$ molar precursor ratio, while SnF_4 is maintained at 5% molar ratio, keeping other reaction parameters identical. The Sn doping level of NCs were characterized by ICP-AES on a Varian 720-ES ICP optical emission spectrometer after digesting the NCs with aqua-regia solution (a mixture of 35% concentrated HCl and 70% HNO_3 in 3:1 ratio respectively).

Lead Sulfide (PbS) Quantum Dot Synthesis: Synthetic procedures by Weidman et al. with standard Schlenk line techniques was used to synthesize PbS quantum dots.[34] Sulfur hot injection solution was prepared in N_2 glovebox with sulfur 20 mg in oleylamine 3.75 ml stirred at 120 °C for 30 min. Lead solution was prepared by adding $PbCl_2$ 2.50 g (9 mmol) with oleylamine 7 ml in three-neck flask. The solution was degassed at 120 °C for 30 min and pressurized with N_2 until temperature was stable. 2.25 ml (0.375 mmol) of prepared sulfur solution was swiftly injected into lead solution and grown for 5 min. Washing procedure was repeated 3 times by dispersion in 20 ml hexane, precipitation with alcohol antisolvents (10 mL butanol, 5 ml methanol), and centrifugation at 4000 rpm for 5 min. Oleic acid 2 ml was added in between wash steps for colloidal stability. Excess $PbCl_2$ precipitates were centrifuged out at 4000 rpm for 3 min and PbS quantum dot supernatant in hexane kept as stock solution.

Film Fabrication: Diced (1 x 1 cm^2) undoped silicon (Si) substrate was sonicated in solvents for 30 min by the following order: Hellmanex-III (5% volume) in deionized (DI) water, DI water rinse prior to next step, acetone, isopropyl alcohol, and hexane. Diluted PbS quantum dot solution (5 mg/ml) in hexane:octane 1:1 by solvent volume was spincoated onto Si substrate at 1500 rpm for 90 sec, then at 4000 rpm for 2 min for drying, providing monolayer PbS film fabrication. F,Sn:In_2O_3 NC monolayer over PbS film was fabricated by modification of liquid-air interface assembly by Dong et al.[37,38] Teflon well (2 × 4 × 4 cm^3) was custom made with ball valve at trough bottom to minimize liquid-air interface perturbation during liquid drainage. PbS quantum dot on Si substrate placed on elevated (1 cm) Teflon platform was immersed in ethylene glycol subphase. 100 µl of dilute F,Sn:In_2O_3 NC solution dispersed in hexane (1 mg/ml) was dropcast onto subphase surface with pipette, and trough was covered with glass slide. F,Sn:In_2O_3 NC monolayer self-assembly was allowed to proceed while hexane gradually evaporated for duration of 15 min. Subphase ethylene glycol was allowed to drain out of the trough well bottom by opening ball valve with minimal self-assembled NC film perturbation. Residual ethylene glycol on film substrate was dried in room temperature vacuum oven for 24 h. Same procedure was used for NC array fabrication over SiN TEM grid, but with absence of PbS quantum dots. Surface organic ligands were removed by plasma cleaning under Ar in excess of 15 min for TEM grid samples.

UV-Vis-NIR/FTIR Spectra Measurement: UV-Vis-NIR spectral measurement was conducted through Agilent Cary 5000 UV−Vis−NIR spectrophotometer, FTIR spectral measurement was conducted through Bruker Vertex 70 FTIR at 4 cm^{-1} scan resolution for solution and film measurement. Hexane dispersed NC solutions were vacuum dried, redispersed in tetrachloroethylene (TCE), and loaded into KBr window 0.05 cm pathlength liquid cell for solution dispersion UV-Vis-NIR and FTIR measurement.

X-ray Diffraction Analysis: X-ray diffraction (XRD) are prepared by drop-casting 20 mg/mL solution of F,Sn:In_2O_3 NCs on Si substrate. The data is collected with a Rigaku MiniFlex 600 X-ray diffractometer using Cu Kα radiation (1.54 Å). Resolved (222) diffraction peak was measured in Rigaku R-Axis Spider diffractometer using Cu Kα radiation at 1.54 Å, with NC powder mounted in mineral oil loaded Kapton loop. Rietveld refinement was further conducted through GSAS-II software.[47]

Electron Microscopy: F,Sn:In_2O_3 NCs are characterized by Hitachi S5500 scanning electron microscope (SEM). Particle size analysis is done with ImageJ with 100 particle count. High resolution transmission electron microscopy (HRTEM) image and selected area electron diffraction (SAED) are acquired with JEOL 2010F TEM at 200kV. Elemental spectrum acquisition of F,Sn:In_2O_3 cubes dropcast on silicon substrates was carried out using a Hitachi S5500 SEM with a Bruker XFlash EDX detector attachment at 5 kV. Elemental deconvolution was performed with Bruker Quantax software reference at zero-tilt angle P/B-ZAF correction.

X-ray Photoelectron Spectroscopy (XPS): Samples were prepared by drop casting NC solutions on a silicon substrate and the measurements were performed in a Kratos Axis Ultra DLD spectrometer with a monochromatic Al Kα source (1486.6 eV). Wide survey scans were acquired at analyzer pass energy of 80 eV and the high-resolution narrow region scans were performed at a pass energy of 20 eV with steps of 0.1 eV. Spectral acquisitions were performed with photoelectron take-off angle at 0° with respect to the surface normal and pressure in the analysis chamber maintained at around 10^{-9} torr. Data analysis was performed in CasaXPS software using the Kratos relative sensitivity factor library. The binding energy (BE) scale was internally referenced to the C 1s peak (BE for C-C = 284.8 eV).

Grazing Incidence Small-Angle X-ray Scattering (GISAXS): Grazing incidence small-angle X-ray scattering was performed using a SAXSLAB Ganesha SAXS system. Assembled NC film samples on Si substrates were loaded in SAXS system vacuum chamber. Monochromatic X-ray radiation of wavelength of 1.54 Å was used. The incident angle of the beam was 0.2°. Small-angle scattered photons were collected with a PILATUS3 R 300K detector with 487 × 619 pixels and a pixel size of 172 μm × 172 μm positioned at the appropriate distances from the sample (1084 mm for GISAXS).

Time-resolved Photoluminescence: The samples were pumped with a Coherent Chameleon Ultra Ti:sapphire laser operating at 850 nm and 5 MHz rep rate, down-converted from 80 MHz using an AOM-based pulse-picker. Excitation and collection was done in reflection geometry using a Mitutoyo NIR 0.42 NA long working distance objective. The collected emission was then sent to a fiber-coupled superconducting nanowire single photon detector (SNSPD) from Single Quantum. Histogram of the SNSPD signal output was done using a PicoQuant HydraHarp 400 Picosecond event timer triggered by the AOM pulse-picker.

Scanning Transmission Electron Microscopy - Electron Energy Loss Spectroscopy (STEM-EELS). Plasmon near-field mapping was performed in a Nion high energy-resolution monochromated STEM- EELS at Oak Ridge National Laboratory operated at 60 kV and a Nion prototype spectrometer.[43,44] Identical energy resolution of 186 cm^{-1} (23 meV) was set to optimize the resolution between the plasmon peaks and the signal in the monochromated beam. Non-negative matrix factorization (NMF) routine available in the Python HyperSpy library was used for plasmon mode deconvolution.

Discussion.

F,Sn:In_2O_3 NC Synthesis. The shapes of the F,Sn:In_2O_3 NCs were controlled by varying the molar ratio of SnF_4 to $Sn(ac)_4$ precursors added to the injection solution. This determines the extent of fluorine and tin dopant incorporation into the resulting NCs product. F,Sn:In_2O_3 NCs with well-defined morphology were produced for 0–3% SnF_4 in the growth solution, as exhibited in Figure 1a. SEM images show that monodisperse NCs cubic morphology were obtained exclusively in the presence of SnF_4 at this dopant range. By comparison, synthesis in the absence of SnF_4 and exclusively with $Sn(ac)_4$ dopant precursor was conducted. Spherical Sn:In_2O_3 NCs were observed (Figure S1), implicating fluorine plays a faceting role in shaping cubic Sn:In_2O_3 NCs. It was observed higher amounts of SnF_4 led to deterioration of cubic NC morphology by forming rough facets. Under absence of $Sn(ac)_4$ precursors, the cube morphology is retained at adequate concentrations of SnF_4 (3% and 5%). Yet, NCs evident with rough surface attributable to F^- ion induced corrosion pitting[18,22] is observed under excessive SnF_4 addition at 10% molar ratio (Figure S2). For the sake of retaining high-quality cube shapes in this study, 5% SnF_4 molar precursor ratio is nominally maintained while further addition of $Sn(ac)_4$ cationic co-doping agent is deliberately controlled for later LSPR tunability.

TEM image of F,Sn:In_2O_3 NC cube from 0% to 3% $Sn(ac)_4$ exhibits a well-defined facet, shown in Figure 1a. Fast Fourier transform (FFT) confirms that F:In_2O_3 NC cubes are single crystalline particles and allows indexing of dominant surface exposed facet (Figure 1a, inset). Observations show the cube is terminated with {100} facets of the In_2O_3 cubic bixbyite structure, consistent with previously reported fluorine passivated In_2O_3 NCs.[7] Crystallinity in NC is well retained at the full $Sn(ac)_4$ dopant range as shown in FFT patterns collected down the <100> zone axis. It is observed rounded cube morphology appears above a threshold 4% $Sn(ac)_4$, until NC become dominantly spherical in shape near 10% $Sn(ac)_4$. The size of NCs remained consistent with edge-to-edge length at 12.6 ± 0.6 nm size range (Figure S3), when synthesized with 10 ml precursor solution injection while $Sn(ac)_4$ dopant precursor ratio was controllably incremented. Versatility in NC cube size control is demonstrated when precursor solution between 1 to 20 ml is controllably injected into hot oleyl alcohol solution. The cubic shape is retained as observed in F,Sn:In_2O_3 NC cube (3% $Sn(ac)_4$) SEM images, following expected injection volume to edge-to-edge NC size trend (Figure S4). Monodispersity is retained while size distribution broadening from 0.6 to 2.4 nm is observed when volume of precursor solution is progressively increased.

To quantify total F and Sn dopant incorporation in F,Sn:In_2O_3 NCs, inductively coupled plasma-atomic emission spectroscopy (ICP-AES) and energy dispersive X-ray (EDX) spectroscopy was conducted. Since the emitted X-rays has high energy after electron beam penetration, EDX has an effective probe depth of about 200 nm, so the results reflect the F composition of the NC ensemble in the drop-casted sample.[7,48] Atomic component quantification (Figure 1b, Figure S5) show F atomic composition being sustained in F,Sn:In_2O_3 NCs around 6.5 at.% as SnF_4 fluorine precursor concentration employed during synthesis is maintained at 5% molar ratio. Sn peak signatures being close vicinity of In peaks in EDX, ICP-AES trace metal elemental analysis was employed for Sn dopant quantification. Sn atomic composition in NC is observed to systematically increase as a function of $Sn(ac)_4$ precursor addition (0 to 15%), demonstrating the efficacy of Sn cationic dopant incorporation into NC. The Sn dopant incorporation into NC show monotonic increase as $Sn(ac)_4$ is proportionally increased in the precursor injection solution. Higher abrupt Sn dopant incorporation observed between 0 and 1% $Sn(ac)_4$ level can be attributed to effective liberation of Sn in soft binding $Sn(ac)_4$ acetate ligands as compared to harder binding halides in SnF_4 dopant precursor only conditions.[49,50]

NC Surface Characterization. Fluoride anions (F^-) have been described as facet-directing agents in metal oxide NCs,[22] exemplified in the fluorinated synthesis of TiO_2 NCs[51,52], F doped F:In_2O_3,[7] and Sn co-doped F,Sn:In_2O_3 NCs[6]. Metal fluoride precursors, such as SnF_4, decompose into HF in the presence of oleic acid during the reaction, releasing fluoride anions and passivating the In-O surfaces with In-F bonds.[51] Walsh et al. previously determined through density functional theory (DFT) calculations that for bixbyite In_2O_3, relaxed {111} facets are energetically preferred over oxygen terminated {100} facets ($\gamma_{(111)} < \gamma_{(100)}$).[53] However, surface-passivation by F^- in metal oxide NCs can be expected to alter the energetic sequence of the facets: F^- passivation of the {100} facets results in surface energy inversion ($\gamma_{(111)} > \gamma_{(100)}$).[52] Correspondingly, F^- functions as a favorable {100} facet capping agent over {111} surface in the bixbyite In_2O_3 NCs, hindering In atomic layer growth at the F^- terminated {100} surface. This directs the synthesis of well-defined F:In_2O_3 cube

NCs previously elucidated when sufficient F^- passivation occurs at the {100} facet.[7]

Observation through electron microscopy strongly indicate that F function as a facet-directing agent in the synthesis of F,Sn:In_2O_3 NCs, and XPS was used to further probe the presence of F on their surfaces (Figure 1c, Figure S5). XPS is sensitive to surface composition, since the escape depth of photoelectrons is only a few nanometers.[54] The existence of F on the F,Sn:In_2O_3 NC surface is revealed by XPS spectra acquired in the In 3p and F 1s regions (Figure 1c). The F 1s peak at 684.6 eV, flanked by the In 3p doublet peaks, retain surface F 1s peak signal intensity as fluorine precursor concentration is maintained at 5% SnF_4 in NC synthesis. As shown in Figure S6, In $3d_{5/2}$ signal components are assignable to lattice In-O (444.3 eV), In-OH (445.0 eV), and In-F (445.8 eV) species.[7,55] O 1s signal components are assignable to lattice oxygen (530.0 eV), oxygen adjacent to oxygen vacancies or other charged defects, such as F_O (531.0 eV), surface hydroxyl (531.8 eV), and carbonyl (533.1 eV) species, respectively.[7,55] The presence of Sn on the NC surface can also be observed through Sn $3d_{5/2}$, indicating co-existence of Sn and F on the NC surface (Figure S6). XPS characterization thus show that fluorine adsorbs on the In_2O_3 NC surfaces, linked to the stability and prevalence of {100} facets in cube-shaped NCs.

The cube shape of F,Sn:In_2O_3 NCs can thus be rationalized through the shape control model demonstrated for halide-passivated NCs.[18,22] The {100} group facet become strongly passivated by F^- capping on the F,Sn:In_2O_3 cube NC surface when adequate SnF_4 fluoride precursor is introduced during NC growth reaction. The NC becomes favorable towards fluorine terminated {100} surface exposure, minimizing total surface energy and resulting in well-defined cube-shaped NCs. Under Sn co-doping, stable surface faceting is observed to be still prevalent in the range of 0 to 3% $Sn(ac)_4$ dopant precursor concentration as observed through XRD (Figure 1d) with prevalence of (400) crystalline index indium oxide bixbyite peak in the drop-casted NC sample. $Sn(ac)_4$ precursor concentration over 4% results in rounding of cube shape until spherical morphology becomes dominant observed in TEM and weaker (400) diffraction peak in XRD. This can be explicated by the difference in preferred surface energy in Sn rich surfaces, as compared to pristine

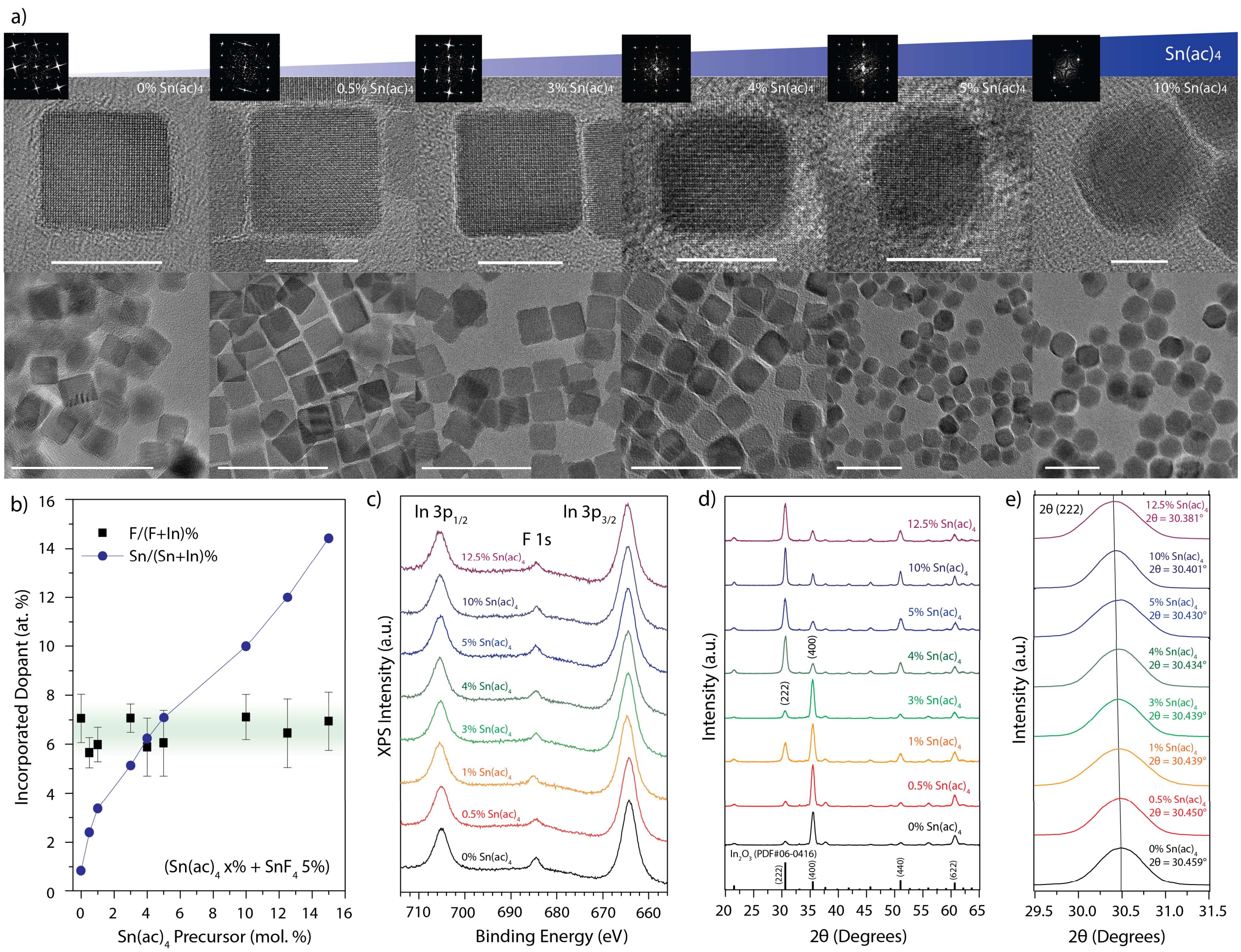

Figure 1. (a) HRTEM image of F,Sn:In_2O_3 NC with progressively increased 0-10% $Sn(ac)_4$ and maintained 5% SnF_4 dopant precursor molar ratio. FFT (inset) show {100} facet orientation of NC cubes, and single particle HRTEM show NC crystallinity (middle) with scale bar at 10 nm. Wide field view HRTEM image scale bar is at 50 nm (bottom). (b) Dopant incorporation in F,Sn:In_2O_3 NC for F and Sn. Fluorine dopant precursor was maintained at 5% SnF_4, with controlled Sn incorporation at 0-15% $Sn(ac)_4$ dopant precursor concentration range. (c) XPS spectra of F,Sn:In_2O_3 NC Sn dopant concentration series for F 1s and In 3p. (d) XRD diffraction pattern of F,Sn:In_2O_3 NCs, (222) and (400) peaks labeled with In_2O_3 powder reference pattern (PDF #00-006-0416) (e) XRD diffraction pattern for (222) reflection show peak shift towards lattice expansion as Sn dopant precursor ratio increases.

In_2O_3. Fluorine terminated SnO_2 phase surface is reported to have preferable surface energy stabilization in {102} termination configuration rather than stabilizing {100} surfaces.[56,57] Excessive Sn doping level will make In_2O_3 surfaces prone to forming SnO_2 phase surfaces,[58] leading to perturbed non-{100} facet fluorine terminated NC surface stabilization. Hence results in rounded cube NC morphology at higher $Sn(ac)_4$ concentration (4 - 5%), and spherical NC shape under excessive Sn dopant incorporation (10%) as observed in Figure 1a.

NC Dopant Incorporation. Prevalent in n-type doped metal oxide NC systems,[50,59] substitutional Sn and F dopants incorporated in In_2O_3 NCs can be charge compensated by free electrons. Through additional co-doping of Sn and F in the In_2O_3 lattice, Kröger-Vink defect equilibrium equations demonstrate that deliberate co-doping may promote additional free carriers over a single dopant.[5] The added Sn cationic dopant allow further additional free-carrier compensation beyond previously reported F doped In_2O_3 NCs,[7] leading to LSPR tuning towards higher frequency due to higher free carrier concentration confined within the NC. Sn is a well-established cationic n-type dopant that induces high free electron concentration in tin doped indium oxide ($Sn:In_2O_3$) transparent conductive oxide films.[60,61] Substitutional F dopants incorporated in the NCs can also be charge compensated by free electrons. F is a similarly established anionic n-type dopant analogue to Sn, inducing a high free electron concentration in fluorine doped tin oxide ($F:SnO_2$) transparent conductive oxide films.[60,61] A Kröger-Vink defect notation equation[62] demonstrates that deliberate In site substitution by Sn cation (Eq. 1), and substitution of O site by F anion (Eq. 2) induce one free electron per site.[63,64]

$$(2\mathrm{Sn}_{\mathrm{In}} \cdot \mathrm{O}_{\mathrm{i}})^{\times} \rightarrow \mathrm{Sn}_{\mathrm{In}}^{\bullet} + (2\mathrm{Sn}_{\mathrm{In}} \cdot \mathrm{O}_{\mathrm{i}}) + \tfrac{1}{2}\mathrm{O}_{2\,(g)} + 2e' \qquad \text{(Eq. 1)}$$

$$\mathrm{In}_{\mathrm{In}}^{x} + 3\mathrm{O}_{\mathrm{O}}^{x} \xrightarrow[\mathrm{In}\ _3]{} 2\mathrm{In}_{\mathrm{In}}^{x} + 3\mathrm{F}_{\mathrm{O}}^{\bullet} + \tfrac{3}{2}\mathrm{O}_{2\,(g)} + 3e' \qquad \text{(Eq. 2)}$$

It is expected incorporation and extent of dopant impurities can affect structural straining within the crystalline lattice. The impact on crystal lattice straining when F^- and Sn^{4+} is incorporated into the In_2O_3 NC is observed by analyzing XRD as a function of Sn incorporation. $F,Sn:In_2O_3$ NCs (1 - 12.5% $Sn(ac)_4$) XRD patterns confirm the cubic bixbyite In_2O_3 crystal structure is well maintained throughout Sn dopant increments (Figure 1d).[65] Fluorine crystal ionic radius of F^- (1.19 Å) being smaller than the O^{2-} site (1.28 Å) in bixbyite phase In_2O_3,[66] would induce lattice contraction when occupying oxygen sites.[5,60] With Sn^{4+} (0.83 Å) ionic radii being smaller than In^{3+} (0.94 Å), Sn^{4+} cation substituting In^{3+} lattice sites would also expect lattice contraction to occur.

However, lattice expansion was observed instead of the expected lattice contraction role of F^- and Sn^{4+} when XRD peak shift was analyzed through Rietveld refinement. XRD pattern revealed the subsequent displacements of the (222) reflections that correspond to lattice expansion induced by Sn^{4+} doping (Figure 1e). Through Vegard's Law fit, the y-intercept for $F,Sn:In_2O_3$ NC is at 10.164 Å, indicative of an expanded lattice constant when assuming Sn dopants are not present in lattice (Figure S7). This is larger than the reported bulk In_2O_3 value of $a = 10.119$ Å.[67] Thus, lattice expansion is observed to occur at high dopant concentrations in $F,Sn:In_2O_3$ NCs, with similar structural trends reported in $F:SnO_2$ and $Sn:In_2O_3$ films.[58,68] This can be explained by electronic repulsion of doped impurity centers when free carriers are excessively procreated within the lattice, as observed in bulk tin doped indium oxide by Köstlin et al.[58] The observed trend indicate high concentration of free electron carriers are available and localized within co-doped $F,Sn:In_2O_3$ NCs, favorable for tuning LSPR optical response in higher energy IR regions.

$F,Sn:In_2O_3$ NC LSPR Optical Properties. LSPR spectral tuning is achieved by dopant incorporation control, with incremental addition of Sn resulting in procreation of free carriers (Eq 1.) leading to higher free

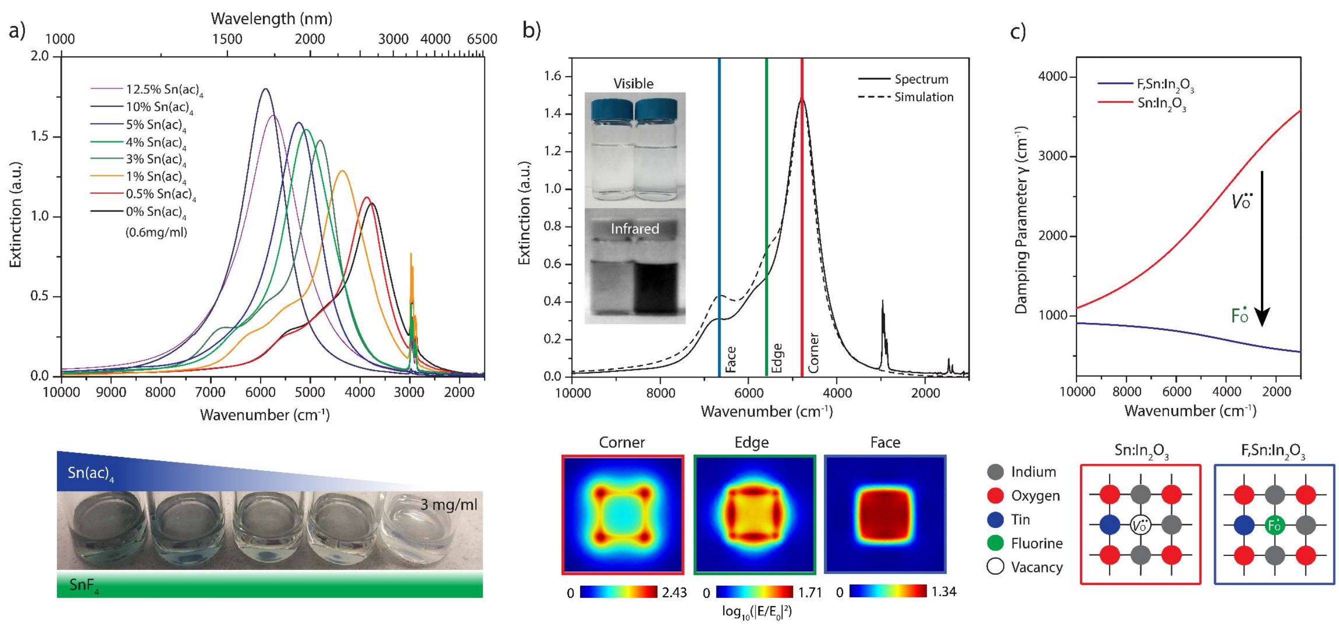

Figure 2. (a) $F,Sn:In_2O_3$ NC UV-Vis-NIR/FTIR extinction spectra. Tunable blueshifted LSPR response is observed as $Sn(ac)_4$ dopant concentration is increased, until blueshift saturate beyond 10% $Sn(ac)_4$. (bottom) Photograph of hexane dispersed $F,Sn:In_2O_3$ NCs (3 mg/ml) solution (0 - 5% $Sn(ac)_4$, left to right). (b) UV-Vis-NIR/FTIR measured extinction spectra (solid line) for $F,Sn:In_2O_3$ (3% $Sn(ac)_4$) NC cube, and simulated extinction spectra curve (dotted line). (inset) IR camera photograph of hexane at left, and dispersed $F,Sn:In_2O_3$ NC 3% $Sn(ac)_4$ (0.1 mg/ml) in hexane at right demonstrating extinction in the IR. (bottom) Near-field maps showing FEM simulated corner (left), edge (middle), and face (right) modes, with 4800 cm^{-1} corner, 5600 cm^{-1} edge, and 6600 cm^{-1} face centered eigenmodes respectively. (c) Extended Drude model damping parameter extracted from extinction spectra for $F,Sn:In_2O_3$ 3% $Sn(ac)_4$ NC (blue) demonstrate low damping, benchmarked to damping parameters from $Sn:In_2O_3$ NC (red) at similar plasma frequency. (bottom) Schematic of F dopant monovalent ionized impurity occupying divalent oxygen vacancy center, suppressing ionized impurity scattering in indium oxide lattice.

charge carrier concentration confined within the NC.[69] With the naked eye, the NC dispersion solution is observably bluer in color as Sn dopant is increased (Figure 2a, bottom). UV-Vis-NIR spectra observations show blueshifting of LSPR extinction spectra as $Sn(ac)_4$ dopant precursor is increased (Figure 2a). At a high Sn dopant concentration window (4 - 15% $Sn(ac)_4$), the NC shape morphology is progressively spherical in shape leading to observation of a single mode LSPR peak characteristic of sphere shaped plasmonic nanoparticle ensemble. At a lower 0 - 3% $Sn(ac)_4$ dopant concentration, a well-defined multimodal peak is observed arising from the cubic NC morphology.[7] The faceting effect of F dopant in this window allows cube NC morphology to be retained while Sn is incrementally doped within the low dopant concentration window range.

$$\epsilon_p = \epsilon_\infty - \frac{\omega_p^2}{\omega^2 + i\gamma\omega} \qquad \text{(Eq. 3)}$$

$$\gamma = \gamma_L - \frac{\gamma_L - \gamma_H}{\pi}\left[\arctan\left(\frac{\omega - \gamma_X}{\gamma_W}\right) + \frac{\pi}{2}\right] \qquad \text{(Eq. 4)}$$

The optical properties in plasmonic metal oxides are determined by the dielectric function (Eq. 3), colloquially known as permittivity. It is treated with the Drude model for a collective free electron gas oscillation under an externally applied electromagnetic field. This consists of plasma frequency ω_p, dependent on the free electron concentration n_e localized within the NC, while perturbing the high frequency dielectric background ϵ_∞ well applied in $Sn:In_2O_3$.[15,69,70] The relation between plasma frequency and free electron concentration $\omega_p = \sqrt{\frac{n_e e^2}{\varepsilon_0 m^*}}$, where n_e is the free electron concentration, e is the elementary electronic charge, ε_0 is the permittivity of free space, and m* is the effective mass, allows assessment of free carrier concentration within the NC bulk domain.[6,70] The extended Drude model (Eq. 4) provides access in assessing ionized impurity scattering contributions within the NC bulk domain.[71,72] Under external electromagnetic oscillation frequencies lower than the plasma frequency, an oscillating free electron is heavily influenced by screened ionized impurity scattering effectively akin to an direct current electrical field.[69] This is manifested by intrinsic divalent ionized oxygen vacancy donors[70] and substitutional monovalent dopant ions ($\mathrm{Sn}_{\mathrm{In}}^{\bullet}$ and $\mathrm{F}_{\mathrm{O}}^{\bullet}$) in the synthesized NC,[6,69] leading to changes in γ_L low frequency damping. Transiting into high-frequency regime and above crossover frequency γ_X, the free electron cloud no longer behave coherently to local ionized impurity centers, leveling off to a constant high frequency γ_H damping value due to reduced scattering probability at higher oscillatory frequency.[69,73]

Prior to multimodal peak assessment in cubic NCs, single peak spectrum fit was conducted using the extended Drude model. Experimentally collected spherical 10% $Sn(ac)_4$ NC spectrum was fitted through MATLAB, implementing extended Drude model and reduced square method to extract free carrier determined plasma frequency ω_p and impurity scattering influenced frequency dependent damping parameters γ_H at high and γ_L at low frequencies.[74,75] Plasma frequency parameter extraction allowed assessment of free carrier concentration of n_e= 1.15 × 10^{21} cm^{-3} within the NC. The plasma frequency of ω_p = 17155 cm^{-1} in this $F,Sn:In_2O_3$ NC allowed noticeable blue-shifting over previous highly doped $Sn:In_2O_3$ NCs at ω_p = 15841 cm^{-1},[74] associable to anionic fluorine co-doping influencing additional free carriers in $F,Sn:In_2O_3$ NCs.[6,7] Additional spectral simulation was conducted with finite element method (FEM) through COMSOL wave design module inputting MATLAB extracted dielectric function parameters, achieving exacting absorption dominant optical spectrum feature between FEM and numerical extended Drude model in spherical NCs (Figure S8).

Shape induced LSPR modes become dominant in well-faceted cubic particles, with oscillatory near-field eigenmodes becoming apparent in corner, edge, and face shape features in single particle NCs.[17] To simulate the multimodal extinction spectra in cubic shaped $F,Sn:In_2O_3$ NCs, FEM based COMSOL wave design module was iteratively refined with extended Drude model initial parameter from MATLAB least square methods.[6,75] A spectrum simulating the three distinct LSPR modes induced by shape observed in the UV-Vis-NIR extinction spectra (Figure 2b) was able to be obtained in $F,Sn:In_2O_3$ (3% $Sn(ac)_4$) NC, with the main peak observed at 4750 cm^{-1} attributed to the corner mode (red), 5600 cm^{-1} the edge mode (green), and 6600 cm^{-1} the face mode (blue). Incremental addition of Sn induces free carriers described by Eq. 1 within the $F,Sn:In_2O_3$ NCs, and from the extracted plasma frequency the free carrier concentration was correlated to n_e= 1.15 × 10^{21} cm^{-3}. In $F,Sn:In_2O_3$ NCs under variant Sn dopant precursor levels, the free carriers in NCs are observed to increase as Sn dopants are further incorporated into the NC until observed blue-shifting saturates at maximum observed value of n_e= 1.32 × 10^{21} cm^{-3} and red-shifts above 10% $Sn(ac)_4$ (Table 1). This demonstrates the viability of LSPR tuning in faceted NCs through synthetic dopant incorporation control, while the cubic shape is retained within the range of fluorine induced faceting effects.

$F,Sn:In_2O_3$ NC	ω_{LSPR} (cm^{-1})	n_e (cm^{-3})	Q
0% $Sn(ac)_4$	3744	0.69 × 10^{21}	3.59
0.5% $Sn(ac)_4$	3845	0.74 × 10^{21}	4.04
1% $Sn(ac)_4$	4338	0.94 × 10^{21}	3.77
3% $Sn(ac)_4$	4789	1.15 × 10^{21}	5.22
4% $Sn(ac)_4$	5066	1.17 × 10^{21}	4.26
5% $Sn(ac)_4$	5216	1.25 × 10^{21}	2.65
10% $Sn(ac)_4$	5858	1.32 × 10^{21}	5.61
12.5% $Sn(ac)_4$	5737	1.26 × 10^{21}	4.33

Table 1. $F,Sn:In_2O_3$ NC (0 - 12.5% $Sn(ac)_4$) dopant series LSPR spectral peak position (ω_{LSPR}), free carrier concentration (n_e), and NC quality factor (Q) value.

The damping parameter under low-frequency regime reveals F co-doping allows narrower LSPR modes as compared to only Sn doped In_2O_3 (Figure 2c). Damping parameter (Eq. 4) consists of low frequency damping γ_L manifests the internal scattering of free electrons.[70,74] As the scattering cross section in ionized impurity scattering is proportional to the square of the ionic charge (Z^2), fluorine induced substitutional $\mathrm{F}_{\mathrm{O}}^{\bullet}$ defects procreated by Eq. 2, occupy divalent oxygen vacancy site $\mathrm{V}_{\mathrm{O}}^{\bullet\bullet}$ and allow suppressed ionized impurity scattering to occur within the co-doped $F,Sn:In_2O_3$ NCs (Figure 2c, bottom).[6,69] As compared to fluorine absent uniformly doped $Sn:In_2O_3$ NCs previously reported in literature,[74] the damping parameter in fluorine present $F,Sn:In_2O_3$ (3% $Sn(ac)_4$) NCs is observed to have significantly lower damping coefficient of γ_L= 585 cm^{-1} (Figure 2c). Similarly, $F,Sn:In_2O_3$ NCs at various Sn dopant precursor levels consistently demonstrate reduced impurity scattering near γ_L = 650 cm^{-1} between 0-10% $Sn(ac)_4$ range (Table S1). In uniformly doped $Sn:In_2O_3$ NCs, ease of $(\mathrm{Sn}_{\mathrm{In}}^{\bullet} - \mathrm{O}_{\mathrm{i}}^{''})^{\mathrm{X}}$ oxygen interstitial defect incorporation in the NC causes noticeable ionized impurity scattering induced damping in the low frequency regime. Previous work demonstrated damping parameters approach that of oxygen vacancy ($\mathrm{V}_{\mathrm{O}}^{\bullet\bullet}$) doped In_2O_3 at the range of 1000 cm^{-1} in surface segregated Sn dopant incorporation onto NC surface, with core of the NC prevalently Sn deficient.[58,76] Damping parameter in fluorine incorporated $F,Sn:In_2O_3$ NCs are agreeably less than reported values in these surface segregated $Sn:In_2O_3$ NCs, due to replacement of $\mathrm{V}_{\mathrm{O}}^{\bullet\bullet}$ divalent oxygen vacancy with $\mathrm{F}_{\mathrm{O}}^{\bullet}$ monovalent ionized defect incorporation. Such improved reduced ionized scattering performance allows maintaining high NC quality factor $Q = \frac{\omega_{LSPR}}{\kappa}$ in Table 1, where narrow spectral linewidth κ and high energy

LSPR peak frequency ω_{LSPR} is achieved.[77] The narrow peak width advantage allow well-defined shape induced multimodal LSPR peaks to be observed in UV-Vis-NIR spectrum measurements.

With F,Sn:In_2O_3 NCs providing narrow LSPR optical response, it is expected for IR range near-field enhancement (NFE) effects to occur. NFE are noticeably observed in near-field simulations, with intense electromagnetic hot-spots localized at the distinctive morphological features in the NC cube. NFE is observed in cubic F,Sn:In_2O_3 (3% $Sn(ac)_4$) NCs at the geometric corner, edge, and face-centered eigenmodes with NFE factor ($\log_{10}|E/E_o|^2$) values of 2.43, 1.71, and 1.34, respectively (Figure 2b, bottom). At a lower Sn dopant precursor level, F,Sn:In_2O_3 (0% $Sn(ac)_4$) NCs with lower NFE factor values of 2.23, 1.57, and 1.21 is respectively obtained for corner, edge, and face (Figure S9). In spherical F,Sn:In_2O_3 (10% $Sn(ac)_4$) NCs with single LSPR mode, a comparatively

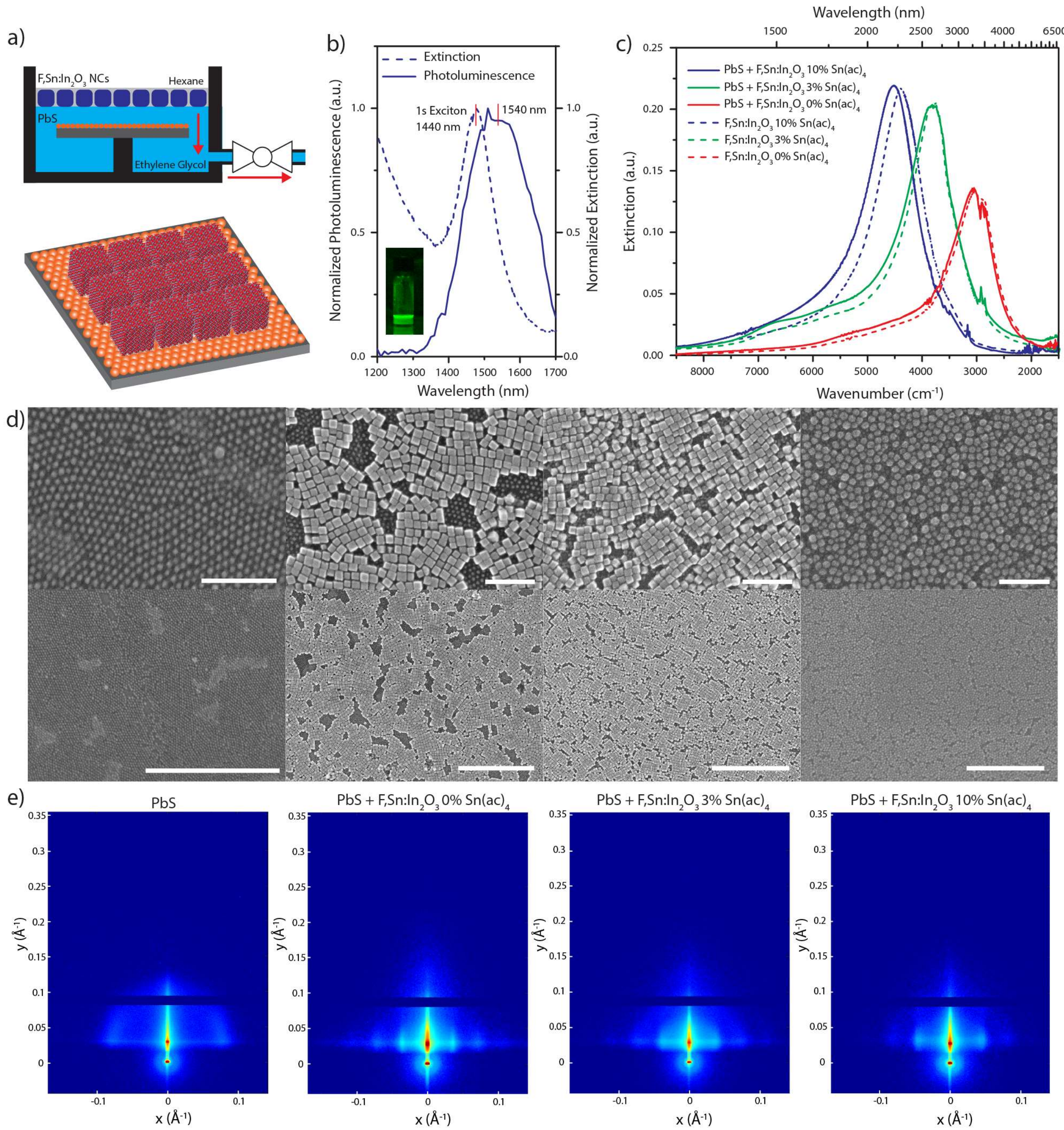

Figure 3. (a) Liquid-air monolayer NC assembly schematic of Teflon trough, hexane dispersed F,Sn:In_2O_3 NC solution on ethylene glycol, and spin-coated PbS quantum dot substrate (top). Ethylene glycol is drained to place monolayer F,Sn:In_2O_3 NCs assembled on top of PbS quantum dot layer (bottom). (b) UV-Vis-NIR spectrum of 1s exciton absorption peak in PbS nanocrystal (dotted) dispersed in tetrachloroethylene with 1540 nm PbS film photoluminescence (solid). IR photo image (inset) show photoemission of PbS sample dispersed in hexane. (c) FTIR extinction spectrum of F,Sn:In_2O_3 NC monolayer assembled film on Si substrate (dotted), and F,Sn:In_2O_3 NC monolayer film overlayered on PbS quantum dot film at Si substrate (solid) exhibiting near unity extinction. (d) SEM image of PbS quantum dot film, and F,Sn:In_2O_3 (0, 3, 10% $Sn(ac)_4$) NC monolayer over PbS film. Bar inset is at 100 nm (top). Wide field SEM image of same film showing monolayer uniformity of film architecture. Bar inset is at 500 nm (bottom). (e) GISAXS of NC monolayer film on Si substrate for (far left) PbS quantum dot, (middle left) F,Sn:In_2O_3 cube (0% $Sn(ac)_4$), (middle right) F,Sn:In_2O_3 cube (3% $Sn(ac)_4$), and (far right) F,Sn:In_2O_3 (10% $Sn(ac)_4$) layered over PbS film. Monolayer NC cube arrays show scattering peak positions corresponding planar array of {100}, {200}, and {300} interparticle ordering indexes.

low NFE value of 1.92 was obtained due to the absence of high-curvature sharp morphological corner features. To further experimentally probe IR near-field effects in ensemble F,Sn:In_2O_3 NC structures, NCs were further selectively assembled into nanocavity architecture arrays.

Monolayer F,Sn:In_2O_3 NC Film Assembly. pectral tunability can be advantageously used in a monolayer NC film array architectures, realizing tunable IR range near-field nanocavity between NC array and substrate without being restricted to particle size dependent tuning.[11] Spectral LSPR tunability in solution dispersed NCs was achieved in the previous section through chemical Sn dopant incorporation control during colloidal synthesis. By assembling LSPR tuned F,Sn:In_2O_3 NC monolayer film onto PbS monolayer film, self-assembled nanocavity can be fabricated, sandwiching PbS quantum dot emitter between substrate and LSPR active cube NC monolayer. To assemble a nanocavity layer over excitonic PbS quantum dots, F,Sn:In_2O_3 cube NC monolayer is fabricated through modification of Dong et al. two-phase assembly method,[37] with immiscible non-polar hexane dispersed NC solution (1 mg/ml, 100 µl) floated on top of polar ethylene glycol solution (Figure 3a, Figure S10). PbS quantum dot monolayer film was fabricated by a dilute hexane-octane dispersed solution (5 mg/ml) spin-coating process. The ethylene glycol subphase layer was drained through a connected ball valve on the Teflon trough bottom. This minimize liquid-air interface perturbation of the self-assembled film after hexane layer is fully evaporated under a glass slide cover.

Dopant controlled tunable LSPR nanocubes show NFE at well-defined morphological features in simulation models. To experimentally probe enhanced electromagnetic field features in F,Sn:In_2O_3 NC arrays, PbS quantum dot emitter probe is used in the film architecture. Emitter probe quantum transition rate dependence between nanocavity electromagnetic field intensity and relation between detuning frequency of LSPR cube array can be experimentally approached, via plasmon-exciton coupling effect. PbS quantum dots are a direct bandgap semiconductor material with tunable IR photoemission response by size dependent quantum confinement.[34,78] PbS quantum dots are synthesized to tune the 1s exciton peak position and correspondingly the PbS film photoluminescence peak frequency (Figure 3b) towards longer wavelengths at F,Sn:In_2O_3 cube NC cavity resonance.[34]

LSPR spectral tunability in self-assembled F,Sn:In_2O_3 NC monolayer film is achieved and characterized through UV-Vis-NIR spectroscopy (Figure 3c). The F,Sn:In_2O_3 and PbS composite film LSPR extinction feature is retained near unity of F,Sn:In_2O_3 NC only film. F,Sn:In_2O_3 cube (0% Sn(ac)$_4$) monolayer assembly show nanocavity mode LSPR peak at ω_{cav} = 3030 cm^{-1}, F,Sn:In_2O_3 cube (3% Sn(ac)$_4$) at ω_{cav} = 3740 cm^{-1}, and F,Sn:In_2O_3 NC (10% Sn(ac)$_4$) at ω_{cav} = 4527 cm^{-1}. Monolayer NC film array show LSPR redshifting due to interparticle plasmon coupling with adjacent NCs when compared with non-interacting TCE solution dispersed NCs. Monolayer F,Sn:In_2O_3 cube (0% Sn(ac)$_4$) arrays show LSPR peak shift of $\Delta\omega_{LSPR}$ = 714 cm^{-1}, F,Sn:In_2O_3 cube (3% Sn(ac)$_4$) at $\Delta\omega_{LSPR}$ = 1049 cm^{-1}, and F,Sn:In_2O_3 NC (10% Sn(ac)$_4$) at $\Delta\omega_{LSPR}$ = 1331 cm^{-1}. The interparticle plasmon coupling resulting in LSPR redshift elude that the NC array form a collective ensemble as a nanocavity that can be probed through PbS emissive lifetime measurement correlation.

SEM image of assembled film show the local ordering in F,Sn:In_2O_3 NC monolayer on PbS quantum dots, with micrometer range uniformity (Figure 3d). The F,Sn:In_2O_3 NC cube (0, 3% Sn(ac)$_4$) monolayer show planar cubic packing while the F,Sn:In_2O_3 NC spheres (10% Sn(ac)$_4$) show monolayer hexagonal packing feature over the PbS layer. The PbS monolayer is maintained after F,Sn:In_2O_3 cube NC monolayer film layer is placed by two-phase solution assembly method (Figure S11). To further characterize the uniformity of film, GISAXS was used to observe the ordering of composite monolayer F,Sn:In_2O_3 cube and PbS quantum dot film (Figure 3e).[37,79] The momentum transfer q scattering from GISAXS is determined by the local Miller index {hkl} ordering and unit cell lattice a of nanocrystal arrays, with relations as $\frac{2\pi}{q} = \frac{a}{\sqrt{h^2+k^2+l^2}}$. The scattering peak intensity in composite F,Sn:In_2O_3 cube monolayer film is consistent to simple cubic lattice array, with unit cell lattice correlating to interparticle NC center distance. For F,Sn:In_2O_3 cube (0% Sn(ac)$_4$), unit cell is measured as a = 17.2 ± 0.3 nm with scattering peak consistent for substrate planar {100}, {200}, and {300} indexes. Higher Sn doped F,Sn:In_2O_3 cubes (3% Sn(ac)$_4$) is observed to have a = 16.7 ± 0.1 nm with identical planar array structure. F,Sn:In_2O_3 NC (10% Sn(ac)$_4$), unit cell is measured as a = 13.4 ± 0.1 nm with scattering peak consistent for planar hexagonal {100}, {111}, and {211} indexes. The PbS composite F,Sn:In_2O_3 NC layer retains interparticle distance and structure when compared to F,Sn:In_2O_3 only monolayer film array (Figure S12). Pristine F,Sn:In_2O_3 cube (0% Sn(ac)$_4$) monolayer array is observed to have interparticle distance of a = 17.5 ± 0.1 nm with substrate planar {100}, {200}, and {300} index array, which is near identical to the previous NC cube overlayered PbS composite film. This is also observed in other pristine films, whith F,Sn:In_2O_3 cube NC (3% Sn(ac)$_4$) interparticle distance at a = 16.8 ± 0.3 nm, and F,Sn:In_2O_3 NC (10% Sn(ac)$_4$) films at a = 13.2 ± 0.4 nm. In pristine PbS quantum dot film, an interparticle distance of a = 8.1 nm is observed. GISAXS reveal F,Sn:In_2O_3 cube monolayer film local architecture observed through SEM, is sufficiently uniform throughout a wide area for further nanocavity spectral characterization.

Plasmon-Exciton Coupling and Nanocavity Probing F,Sn:In_2O_3 cube NCs demonstrate IR range LSPR tunability through UV-Vis-NIR spectroscopy measurements, and exhibit emergent NFE behavior with near-field simulations. This can be extended to realize dopant induced spectrally tunable IR nanocavities in monolayer film architecture which was previously difficult to access in fixed free carrier host materials such as Ag or Au noble metal nanoparticles. By placing PbS quantum dot layer under LSPR active F,Sn:In_2O_3 NC monolayers, quantum dots can be used to realize exciton-plasmon coupling used as a photoluminescence probe to understand tunable IR near-field nanocavities.[41] The decay lifetime (τ_0) is representative of the quantum transition rate from excited to ground state of exciton hole-electron pair recombination in PbS quantum dots. Coupling LSPR induced enhanced near-field with photoluminescent exciton recombination ($\Gamma_0 = \frac{1}{\tau_0}$) leads to accelerated lifetime decay rate ($\Gamma_{tot} = \frac{1}{\tau_{tot}} = \Gamma_0 + \Gamma_{cav}$).[80,81]

$$\Gamma_{cav} = \left(\frac{4g^2}{\kappa}\right)\frac{1}{1+\left(\frac{2\delta}{\kappa}\right)^2} = \Gamma_{tot} - \Gamma_0 \qquad \text{(Eq. 5)}$$

$$g = \frac{1}{2}\sqrt{(\Gamma_{tot} - \Gamma_0)(1+\left(\frac{2\delta}{\kappa}\right)^2)\kappa} \qquad \text{(Eq. 6)}$$

The modulation of electromagnetic field in confined cavity plays influence by enhancing the excited state to ground state transition rate (Γ_{cav}) under Fermi's golden rule, which can be reiterated into the Purcell effect. The coupling strength can be extracted from the experimental photoluminescence lifetime decay rate by Eq. 5. The off-resonance frequency between the plasmonic nanocube monolayer cavity (ω_{cav}) with LSPR cavity linewidth κ, and quantum dot emitter (ω_{emit}) is termed detuning frequency ($\delta = \omega_{cav} - \omega_{emit}$).[80] To assess the interaction strength between LSPR and exciton coupling, Eq. 5 can be reorganized to give coupling strength (g) in Eq. 6.[80,82] Controlled dopant incorporation in NC is especially advantageous, as LSPR frequency can be tuned in the IR, without relying on size induced tuning as in Ag or Au nanoparticles.

Empirical coupling strength is assessed through IR photoluminescence lifetime measurement with stretched exponential decay curve fitting.[41] F,Sn:In_2O_3 cube NC (3% Sn(ac)$_4$) coupled PbS assembly films was observed to have shortened lifetime of $\tau_0 = 0.016$ ns as compared to PbS film at $\tau_0 = 0.365$ ns (Figure 4a). Other case studies are obtained with PbS film (ω_{emit} = 6944 cm^{-1}) coupled to highly off-resonant F,Sn:In_2O_3 (0% Sn(ac)$_4$) NC cubes (ω_{cav} = 3051 cm^{-1}, κ = 28.8 THz). Enhanced lifetime decay was weak at g = 0.99 THz (4.09 meV), indicating limited coupling behavior under high detuning frequency (δ = 3893 cm^{-1}). Upon closer spectral overlap between LSPR nanocavity and excitonic quantum dot emitter, F,Sn:In_2O_3 (3% Sn(ac)$_4$) NC cube monolayer (ω_{cav} = 3808 cm^{-1}, $\kappa = 32.7$ THz) showed enhanced exciton lifetime decay with a coupling strength of g = 4.08 GHz (16.85 meV) at δ = 3136 cm^{-1}. In PbS coupled spherical F,Sn:In_2O_3 (10% Sn(ac)$_4$) NC films (ω_{cav} = 4521 cm^{-1}, κ = 33.3 THz), despite a lower detuning frequency at δ = 2423 cm^{-1} and closer resonant overlap, the coupling strength was observed to be noticeably reduced at g = 1.40 THz (5.78 meV). The narrow cavity linewidth κ at 30 THz range from all monolayer film assembly (Figure 3c) is representative of the photonic mode decay rate, affirming the IR nanocavity architecture is in the weak coupling regime by comparing the coupling strength to cavity linewidth ($g < \kappa$).[82–84] The localized photonic mode in the cavity decays faster than the exciton to LSPR coupled Rabi oscillation,[85] leading to enhanced accessible pathway in photonic modes of decay, and thus enhanced exciton photoluminescence decay rate induced by F,Sn:In_2O_3 NCs.

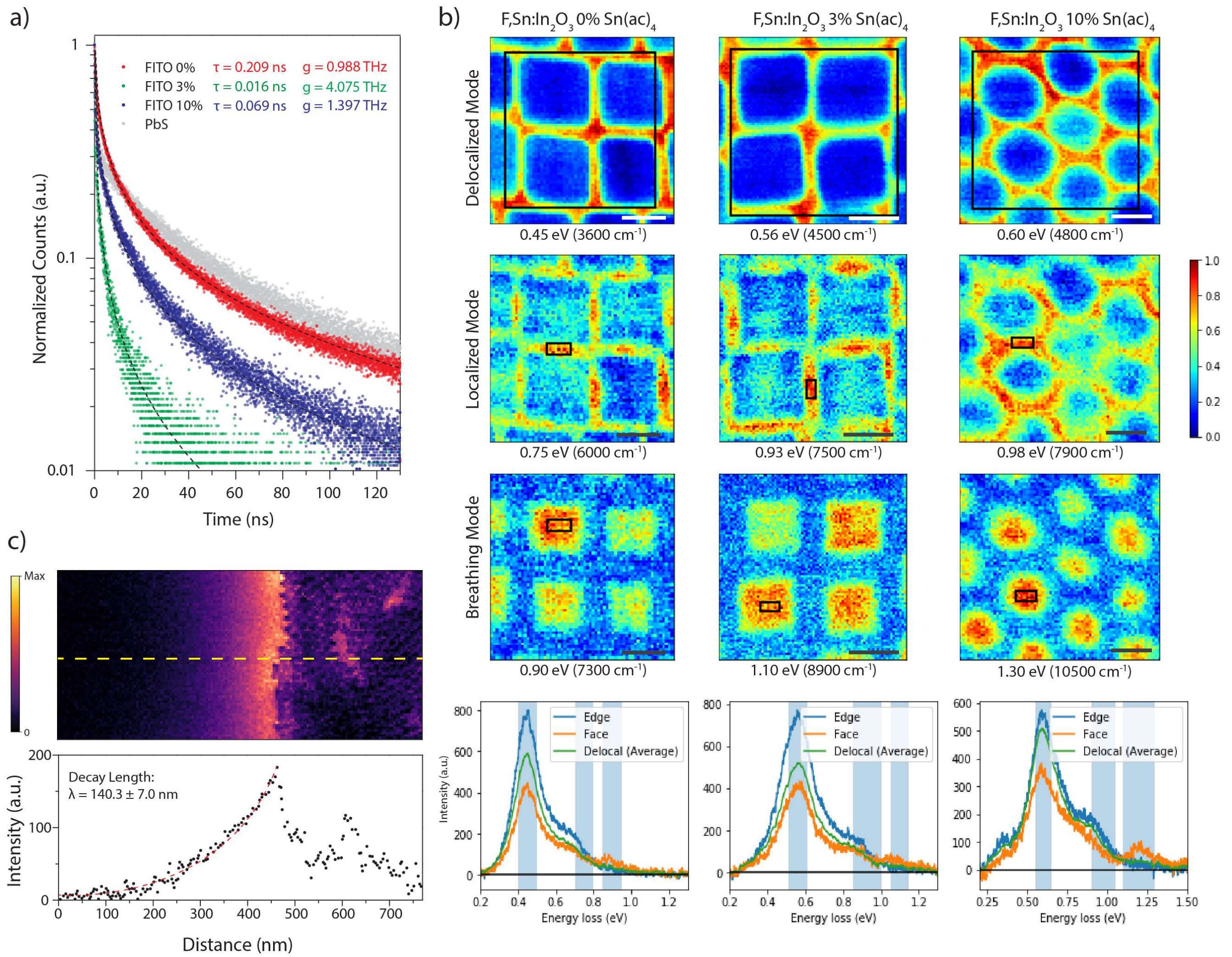

Figure 4. (a) Photoluminescence lifetime measurement of PbS QD film coupled with F,Sn:In_2O_3 NC monolayer assembly nanocavity. Enhanced decay lifetime is observed when LSPR active F,Sn:In_2O_3 NC cube is present. (red) PbS coupled to detuned F,Sn:In_2O_3 (0% Sn(ac)$_4$) NC cube monolayer exhibit weak decay enhancement behavior, while (green) F,Sn:In_2O_3 (3% Sn(ac)$_4$) NC cube monolayer demonstrate high Purcell enhancement. (blue) PbS coupled to spherical F,Sn:In_2O_3 (10% Sn(ac)$_4$) NCs show intermediate decay rate. Laser excitation source was 850 nm on PbS band edge at 25 µW intensity and 5 MHz repetition rate. (b) STEM-EELS near-field intensity map of F,Sn:In_2O_3 NC array. Columns represent (left) F,Sn:In_2O_3 (0% Sn(ac)$_4$) NC cube, (middle) F,Sn:In_2O_3 (3% Sn(ac)$_4$) NC cube, and (right) F,Sn:In_2O_3 (10% Sn(ac)$_4$) NC sphere arrays, with intensity maps normalized to observed mode. Distinct spatially delocalized, interparticle gap edge localized, and NC localized face breathing modes are observed at respective labeled frequencies. Scale bars are at 5 nm. (below) EELS spectra demonstrate near-field tunability, observed in delocalized average mode, localized gap edge, and face breathing mode in demarcated reduced map area for respective F,Sn:In_2O_3 NC array. (c) STEM-EELS near-field map of F,Sn:In_2O_3 (0% Sn(ac)$_4$) NC cube assembly array edge. Linear intensity profile show observation of delocalized LSPR decay length at 140.3 ±7.0 nm.

To further address the nanoscopic localized nature of F,Sn:In_2O_3 cube electromagnetic field coupled to PbS excitons, the Purcell enhancement[86] in Eq. 7 is approached with assistance from simulation models and direct STEM-EELS observations. In free-space, unperturbed by local electromagnetic field environment, the spontaneous emission can be expressed by Eq. 8.[87] From Fermi's golden rule, the hole-electron pair recombination emission rate in quantum transition probability can be perturbed by the local electromagnetic field in a photonic cavity environment. This is described in Eq. 9 as a time-independent term expressed by the enhanced local electromagnetic field (E) and exciton transition dipole moment (μ_{12}).[81,88]

$$F_p = \frac{\Gamma_{tot}}{\Gamma_0} \qquad \text{(Eq. 7)}$$

$$\Gamma_0 = \frac{{\omega_0}^3{\mu_{12}}^2}{3\pi\varepsilon_0\hbar c^3} \qquad \text{(Eq. 8)}$$

$$\Gamma_{tot} = \frac{2\pi}{\hbar^2}|\langle f|\mathrm{d}\cdot \mathrm{E}|i\rangle|^2\rho(\omega_0) = \frac{2\pi}{\hbar^2}|\langle \mu_{12}E\rangle|^2\rho(\omega_0) \qquad \text{(Eq. 9)}$$

The nanocube morphology of infrared LSPR active F,Sn:In_2O_3 NCs allow intense near-field localized resonance due to antenna effects at corners, allowing confinement of light beyond the diffraction limit. In a monolayer assembly array of cubes, the near-field enhancement effect is used to localize high density of IR range light around the PbS quantum dot array in a nanocavity.[26,41] Whereas photonic modes in free space would be broadly distributed throughout a wide frequency range, the infrared LSPR active F,Sn:In_2O_3 NCs allow photonic modes to be localized to a controllably tuned resonant frequency. The photonic density of state ($\rho(\omega_0)$) in a nanocavity is confined and centered to an LSPR resonance frequency (ω_{cav}) of quality factor $Q = \frac{\omega_{cav}}{\kappa}$, expressed as a Lorentzian distribution (Eq. 10) corresponding to experimentally observed LSPR cavity extinction spectra. The confined cavity electromagnetic field (E) is expressed and modified into a normalized volume mode (V) in Eq. 11 for a nanocavity architecture.[87,89,90]

$$\rho(\omega_0) = \frac{2}{\pi\kappa}\frac{\left(\frac{\kappa}{2}\right)^2}{\left(\frac{\kappa}{2}\right)^2 + (\omega_{cav} - \omega_{emit})^2} \qquad \text{(Eq. 10)}$$

$$|\langle \mu_{12}E\rangle|^2 = \frac{{\mu_{12}}^2\hbar\omega_0}{2\varepsilon_0 n^2 V}\xi^2 \qquad \text{(Eq. 11)}$$

Intraband energy dissipation losses commonly observed in Au and Ag nanocavities can be advantageously negated in the doped metal oxide nanocavity system. IR range LSPR resonance separation in frequency space is far apart from band edge loss features located at the visible spectral range.[89,91] Therefore, emitter to cavity detuning components can be expressed into Eq. 12 for fully describing the Purcell enhancement factor F_p. To account for random isotropic orientation between exciton dipole of spherical quantum dot in a cavity, ξ^2 dipole orientation factor of 1/3 is accounted into the Purcell factor expression. The nanocavity confinement of electromagnetic field modify the volume mode (V) in Eq. 13, which is of pure electromagnetic property describing the effectiveness of the nanocavity concentrating electromagnetic field in confined space.[88,92] The local relative field amplitude of cavity mode expressed as $\boldsymbol{E}$ is normalized so that norm is unity at the maximum amplitude antinode of the incident electric field (E_0).[88,89]

$$F_p = \frac{3}{4\pi^2}\left(\frac{\lambda_0}{n}\right)^3\left(\frac{Q}{V}\right)\frac{(\frac{\kappa}{2})^2}{(\frac{\kappa}{2})^2 + (\omega_{cav} - \omega_{emit})^2}\xi^2 \qquad \text{(Eq. 12)}$$

$$V = \frac{1}{\varepsilon_0 n^2}\int \varepsilon(r)|\boldsymbol{E}(r)|^2 d^3r \qquad \text{(Eq. 13)}$$

STEM-EELS allow direct observation and verification of spectrally tunable near-field existing at the assembled LSPR cube array (Figure 4b). Near-field intensity was simulated for the interparticle nanocube facet gaps arising from plasma treatment removal of NC surface ligands. The

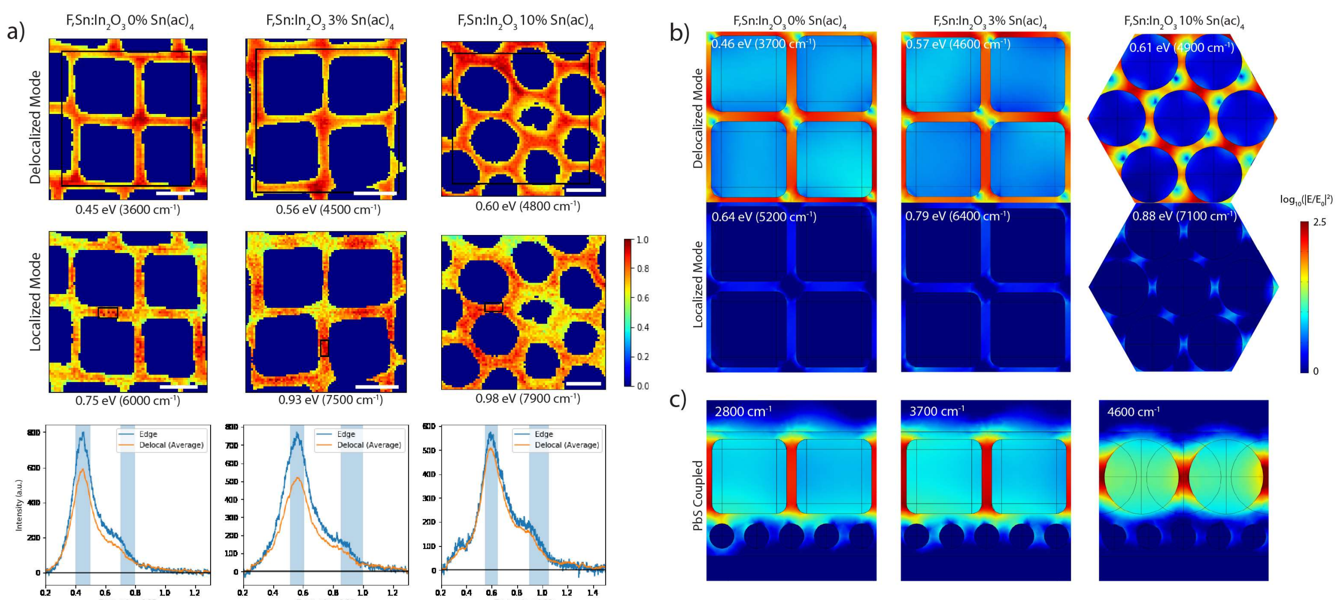

Figure 5. (a) STEM-EELS near-field intensity map of F,Sn:In_2O_3 NC array, with NC area masked to observe NFE intensity. Spatially delocalized and interparticle gap localization is observed at labeled frequencies, intensity map normalized to respective mode. Near-field selective EELS spectra and intensity are plotted below. Scale bars are at 5 nm. (b) Simulated local NFE map of F,Sn:In_2O_3 NC assembly. Top-down view of F,Sn:In_2O_3 NC array interparticle gap simulating STEM-EELS environmental configuration uncoupled to PbS QD. Delocalized (top) and localized (middle) mode NFE maps at respective frequencies observed through STEM-EELS. (c) Cross-section NFE map of coupled nanocavity assembly, with PbS QD coupled between substrate and F,Sn:In_2O_3 NC array. Columns represent (left) F,Sn:In_2O_3 (0% $Sn(ac)_4$) NC cube, (middle) F,Sn:In_2O_3 (3% $Sn(ac)_4$) NC cube, and (right) F,Sn:In_2O_3 (10% $Sn(ac)_4$) NC sphere arrays in b, and c.

emergent delocalized nature of near-field modes was able to be directly observed. Near-field intensity in array assembly is observed to be stronger compared to a single particle in both simulation model and STEM-EELS measurement. In single particle F,Sn:In_2O_3 (10% Sn(ac)$_4$) STEM-EELS, near-field energy loss peak located at 0.8 eV is weak (Figure S14), while a four-fold near-field intensity increase was observed in energy loss peak located at 0.6 eV for assembled NC gap (Figure S15). This observed interparticle gap near-field intensification trends with FEM simulation results. Interparticle NC array gap near-field demonstrate higher NFE enhancement factor ($\log_{10}|E/E_o|^2$) values of 2.35 (Figure 5a,b), while single NC show NFE factor of 1.92 (Figure S9). Secondary higher energy mode centered at 0.85 eV emerge from STEM-EELS mapping in NC film arrays that are attributable to localized gap confined near-field mode (Figure 4b, 5a), while map profile show the main peak mode centered at 0.6 eV is a delocalized near-field ensemble with uniform feature across the array (Figure 4b, 5a). F,Sn:In_2O_3 NC monolayer film series STEM-EELS demonstrate that the near-field is spectrally tunable, noticeable by primary energy loss peak blueshifts under higher Sn doped NCs, while localized secondary mode is also observed in all three F,Sn:In_2O_3 NC assemblies (Figure 4b, Figure S17). High energy breathing mode was observed localized within the NC domain, a nonradiative dark mode that evade light scattering attributed to symmetrical zero net dipole moment, but exclusively observed through EELS technique.[42,93] Through STEM-EELS, long-range plasmonic near-field decay is directly observed at the edge of the assembly (Figure 4c). Simulated NFE enhancement factor values of 2.12 in F,Sn:In_2O_3 (0% Sn(ac)$_4$) NCs and 2.09 in F,Sn:In_2O_3 (3% Sn(ac)$_4$) NC arrays were derived at interparticle nanocube gaps (Figure 5b). Secondary localized modes experimentally observed through STEM-EELS was simulated, with NFE enhancement factor values of 0.34 between the cube facet gap in F,Sn:In_2O_3 (0% Sn(ac)$_4$) NC arrays, 0.36 in F,Sn:In_2O_3 (3% Sn(ac)$_4$) NCs, and 0.68 in F,Sn:In_2O_3 (10% Sn(ac)$_4$) NCs.

Through prior Purcell effect lifetime decay enhancement measurement and near-field intensity, collective electromagnetic volume mode in spectrally tuned NC film is correlated and quantified. The assembled cube array nanocavity local electromagnetic field intensity approached through FEM simulation (Figure 5c) is used to quantify the near-field enhanced electromagnetic field (E) from incident excitation (E_0).[89–91,94] With the PbS quantum dot emitter ($\omega_{emit} = 6944\ cm^{-1}, \lambda = 1540\ nm$), coupled to F,Sn:$In_2O_3$ (3% Sn(ac)$_4$) cube NC cavity ($Q = 3.49$), Eq. 12 components can be evaluated. With locally enhanced electromagnetic near-field simulations under $E_0 = 0.125\ V \cdot m^{-1}$ incident intensity from 25 µW excitation source ($I = \frac{cn\varepsilon_0}{2}|E_0|^2$), the delocalized photonic mode volume of F,Sn:In_2O_3 NC array can be extracted. With the PbS quantum dot placed in a cube to substrate cavity gap, excitonic quantum dots experience an averaged near-field enhancement of E/E_0 = 1.30 (Figure 5c). The number of NCs contributing to the ensemble photonic cavity mode can be numerated,[95] with composing delocalized nanocube volume mode relates to be an averaged 3 × 3 array of F,Sn:In_2O_3 (3% Sn(ac)$_4$) NCs, corresponding to 49 × 49 nm^2 LSPR-exciton coupled real-space delocalization range[96] when nanocavity thickness of 10 nm is assumed. Further detuned F,Sn:In_2O_3 (0% Sn(ac)$_4$) NCs with E/E_0 = 1.35 had an averaged 7 × 7 array of corresponding to 117 × 117 nm^2 delocalization range. For spherical F,Sn:In_2O_3 (10% Sn(ac)$_4$) NC nanocavity ($Q = 4.07$), a lower NFE enhancement of E/E_0 = 1.03 was simulated and delocalized NC cavity array is calculated to be an averaged 5 × 5 NC array, with 76 × 76 nm^2 real-space delocalization range. This is explains observation in FTIR extinction spectra between independent solution dispersed F,Sn:In_2O_3 NCs and redshifted monolayer film assembly. Through the photoluminescence lifetime analysis, it is notable that the local nearfield environment can be probed to quantify the delocalized photonic cavity environment in such monolayer film architecture. The existence of near-field delocalization in the nanocrystal array can be directly observed at the edge of the assembly through STEM-EELS. The intensity of the plasmonic near-field decays exponentially at a decay length of 140.3 ± 7.0 nm (Figure 4c, Figure S20). This further supports that the near-field cavity is not individually confined to one nanocrystal, but an ensemble collective behavior is existent in the nano-assembly array leading to a delocalized nanocavity volume mode approachable through exciton lifetime correlations.

Conclusion

Sn co-doping allows LSPR spectral tunability to be achieved in cubic faceted F doped In_2O_3 NC. F dopant playing a role in selectively passivating {100} crystallographic facet surfaces of In_2O_3 into cubic shaped NCs, deliberate addition of Sn co-dopant precursors routes a synthetic handle in IR range LSPR tunability control. In these colloidally synthesized F,Sn:In_2O_3 NC cubes, shape-dependent LSPR multimodal extinction features arise at the well-defined corner, edge, and face of the NC surface. Expected near-field enhancement effects arise at these morphological features while retaining spectral tunability. The unique dopant induced, size-independent spectral LSPR tunability observed in solution dispersed F,Sn:In_2O_3 NCs can be further exploited through self-assembled films. The tunable near-field effect can be used to fabricate dense plasmonic nanocavity arrays in long-range ordered monolayer architectures, fabricated through liquid-air interface assembly method. IR range photoluminescent PbS QD were coupled with the LSPR near-field tunable F,Sn:In_2O_3 NC nanocavity structure, inducing plasmon-exciton coupling. By controlling the detuning frequency between PbS emitter probe and LSPR active F,Sn:In_2O_3 NC nanocavity, Purcell enhancement in exciton decay rate was achieved. To further understand the spatial near-field nature of assembled NC arrays, direct observation of LSPR near-field was conducted through IR range STEM-EELS mapping. Intense localized near-field was observed between F,Sn:In_2O_3 NC interparticle gap arrays, while and an ensemble plasmonic behavior was emergent. Extensive LSPR delocalization was apparent within and at the edge of F,Sn:In_2O_3 NC array assembly, supported with a delocalized collective volume mode observed through Purcell enhancement analysis.

F,Sn:In_2O_3 NC nanocubes induce strong LSPR near-field response in the IR range, further exploited by creating spatially dense and tunable nanocavity arrays, without relying on size dependent tuning as in conventional Ag and Au noble metal nanomaterials. The optical properties observed in F,Sn:In_2O_3 NCs show potential to be harnessed into photocatalytic applications,[97] ultrafast photonic switching,[41] and plasmonic molecular sensors.[98] Coupling excitonic photoemission and LSPR near-field enhancement, through quantum dot and plasmonic material classes of particles respectively, would enable photonic 'assembly of light' towards hybrid forms of light-matter interaction.[83] By further synthetically tuning LSPR across extended IR spectral range, faceted NCs with enhanced near-fields may show potential in coupling to more IR range exclusive low-energy elementary excitations beyond excitons. These may include phonons,[99] polarons,[100] polaritons,[101] and molecular vibrations,[102] which were previously hard to approach with conventional noble metal classes of nanostructures. Extended synthetic LSPR capabilities in doped metal oxide NCs, including F,Sn:In_2O_3 nanocubes, may provide to become a gateway material for exploring previously unapproached LSPR coupled light-matter interactions and phenomena.

Supplementary Material

See supplementary material for additional information for NC sample SEM, EDX, XPS, XRD, UV-Vis-NIR characterization, extended Drude parameter, and FEM simulated NFE. Additional NC film SEM, SAXS, FEM simulated NFE, and STEM-EELS characterizations are included.

Author Information
Corresponding Author
E-mail: milliron@che.utexas.edu (D.J.M.).

Notes:
The authors declare no competing financial interest.

Acknowledgments
S.H.C., S.G., L.C.R., S. H., K. K., and D.J.M. acknowledge the support from the National Science Foundation (NSF, CHE-1609656, CBET-1704634, NASCENT, an NSF ERC EEC-1160494, and CDCM, an NSF MRSEC DMR-1720595), the Welch Foundation (F-1848), and Fulbright Program (IIE-15151071). We thank K. Jarvis, A. Dolocan, and H. Celio in the Texas Materials Institute (TMI) for user facility assistance. Some microscopy research was performed as part of a user proposal at Oak Ridge National Laboratory (ORNL) the Center for Nanophase Materials Sciences (CNMS), which is a U.S. Department of Energy, Office of Science User Facility (K.M.R., J.A.H.). This research was conducted, in part, using instrumentation within ORNL's Materials Characterization Core provided by UT-Battelle, LLC, under contract No. DE-AC05-00OR22725 with the DOE, and sponsored by the Laboratory Directed Research and Development Program of Oak Ridge National Laboratory, managed by UT-Battelle, LLC, for the U.S. Department of Energy. L.C.R. acknowledges the MMRRSA School at ORNL.

References
(1) Agrawal, A.; Cho, S. H.; Zandi, O.; Ghosh, S.; Johns, R. W.; Milliron, D. J. Localized Surface Plasmon Resonance in Semiconductor Nanocrystals. *Chem. Rev.* **2018**. https://doi.org/10.1021/acs.chemrev.7b00613.
(2) Kanehara, M.; Koike, H.; Yoshinaga, T.; Teranishi, T. Indium Tin Oxide Nanoparticles with Compositionally Tunable Surface Plasmon Resonance Frequencies in the Near-IR Region. *J. Am. Chem. Soc.* **2009**, *131* (49), 17736–17737. https://doi.org/10.1021/ja9064415.
(3) Buonsanti, R.; Llordes, A.; Aloni, S.; Helms, B. A.; Milliron, D. J. Tunable Infrared Absorption and Visible Transparency of Colloidal Aluminum-Doped Zinc Oxide Nanocrystals. *Nano Lett* **2011**, *11*, 4706–4710. https://doi.org/10.1021/nl203030f.
(4) Gordon, T. R.; Paik, T.; Klein, D. R.; Naik, G. V.; Caglayan, H.; Boltasseva, A.; Murray, C. B. Shape-Dependent Plasmonic Response and Directed Self-Assembly in a New Semiconductor Building Block, Indium-Doped Cadmium Oxide (ICO). *Nano Lett.* **2013**, *13* (6), 2857–2863. https://doi.org/10.1021/nl4012003.
(5) Ye, X.; Fei, J.; Diroll, B. T.; Paik, T.; Murray, C. B. Expanding the Spectral Tunability of Plasmonic Resonances in Doped Metal-Oxide Nanocrystals through Cooperative Cation–Anion Codoping. *J. Am. Chem. Soc.* **2014**, *136* (33), 11680–11686. https://doi.org/10.1021/ja5039903.
(6) Agrawal, A.; Singh, A.; Yazdi, S.; Singh, A.; Ong, G. K.; Bustillo, K.; Johns, R. W.; Ringe, E.; Milliron, D. J. Resonant Coupling between Molecular Vibrations and Localized Surface Plasmon Resonance of Faceted Metal Oxide Nanocrystals. *Nano Lett.* **2017**, *17* (4), 2611–2620. https://doi.org/10.1021/acs.nanolett.7b00404.
(7) Cho, S. H.; Ghosh, S.; Berkson, Z. J.; Hachtel, J. A.; Shi, J.; Zhao, X.; Reimnitz, L. C.; Dahlman, C. J.; Ho, Y.; Yang, A.; et al. Syntheses of Colloidal F:In2O3 Cubes: Fluorine-Induced Faceting and Infrared Plasmonic Response. *Chem. Mater.* **2019**, *31* (7), 2661–2676. https://doi.org/10.1021/acs.chemmater.9b00906.
(8) Alvarez, M. M.; Khoury, J. T.; Schaaff, T. G.; Shafigullin, M. N.; Vezmar, I.; Whetten, R. L. Optical Absorption Spectra of Nanocrystal Gold Molecules. *J. Phys. Chem. B* **1997**, *101* (19), 3706–3712. https://doi.org/10.1021/jp962922n.
(9) Naik, G. V.; Shalaev, V. M.; Boltasseva, A. Alternative Plasmonic Materials: Beyond Gold and Silver. *Adv. Mater.* **2013**, *25* (24), 3264–3294. https://doi.org/10.1002/adma.201205076.
(10) Maier, S. A. *Plasmonics: Fundamentals and Applications*; Springer US, 2007.
(11) Ringe, E.; Langille, M. R.; Sohn, K.; Zhang, J.; Huang, J.; Mirkin, C. A.; Van Duyne, R. P.; Marks, L. D. Plasmon Length: A Universal Parameter to Describe Size Effects in Gold Nanoparticles. *J. Phys. Chem. Lett.* **2012**, *3* (11), 1479–1483. https://doi.org/10.1021/jz300426p.
(12) Luther, J. M.; Jain, P. K.; Ewers, T.; Alivisatos, A. P. Localized Surface Plasmon Resonances Arising from Free Carriers in Doped Quantum Dots. *Nat Mater* **2011**, *10*, 361–366. https://doi.org/10.1038/nmat3004.
(13) Agrawal, A.; Kriegel, I.; Milliron, D. J. Shape-Dependent Field Enhancement and Plasmon Resonance of Oxide Nanocrystals. *J. Phys. Chem. C* **2015**, *119* (11), 6227–6238. https://doi.org/10.1021/acs.jpcc.5b01648.
(14) Link, S.; El-Sayed, M. A. Size and Temperature Dependence of the Plasmon Absorption of Colloidal Gold Nanoparticles. *J. Phys. Chem. B* **1999**, *103* (21), 4212–4217. https://doi.org/10.1021/jp984796o.
(15) Mendelsberg, R. J.; Garcia, G.; Milliron, D. J. Extracting Reliable Electronic Properties from Transmission Spectra of Indium Tin Oxide Thin Films and Nanocrystal Films by Careful Application of the Drude Theory. *J. Appl. Phys.* **2012**, *111* (6), 063515. https://doi.org/10.1063/1.3695996.
(16) Xia, Y.; Xia, X.; Peng, H.-C. Shape-Controlled Synthesis of Colloidal Metal Nanocrystals: Thermodynamic versus Kinetic Products. *J. Am. Chem. Soc.* **2015**, *137* (25), 7947–7966. https://doi.org/10.1021/jacs.5b04641.
(17) Nicoletti, O.; Peña, F. de la; Leary, R. K.; Holland, D. J.; Ducati, C.; Midgley, P. A. Three-Dimensional Imaging of Localized Surface Plasmon Resonances of Metal Nanoparticles. *Nature* **2013**, *502* (7469), 80–84. https://doi.org/10.1038/nature12469.
(18) Xia, X.; Xie, S.; Liu, M.; Peng, H.-C.; Lu, N.; Wang, J.; Kim, M. J.; Xia, Y. On the Role of Surface Diffusion in Determining the Shape or Morphology of Noble-Metal Nanocrystals. *Proc. Natl. Acad. Sci.* **2013**, *110* (17), 6669–6673. https://doi.org/10.1073/pnas.1222109110.
(19) Meyns, M.; Iacono, F.; Palencia, C.; Geweke, J.; Coderch, M. D.; Fittschen, U. E. A.; Gallego, J. M.; Otero, R.; Juárez, B. H.; Klinke, C. Shape Evolution of CdSe Nanoparticles Controlled by Halogen Compounds. *Chem. Mater.* **2014**, *26* (5), 1813–1821. https://doi.org/10.1021/cm4037082.
(20) Ghosh, S.; Gaspari, R.; Bertoni, G.; Spadaro, M. C.; Prato, M.; Turner, S.; Cavalli, A.; Manna, L.; Brescia, R. Pyramid-Shaped Wurtzite CdSe Nanocrystals with Inverted Polarity. *ACS Nano* **2015**, *9* (8), 8537–8546. https://doi.org/10.1021/acsnano.5b03636.
(21) Liu, G.; Yang, H. G.; Pan, J.; Yang, Y. Q.; Lu, G. Q. (Max); Cheng, H.-M. Titanium Dioxide Crystals with Tailored Facets. *Chem. Rev.* **2014**, *114* (19), 9559–9612. https://doi.org/10.1021/cr400621z.
(22) Ghosh, S.; Manna, L. The Many "Facets" of Halide Ions in the Chemistry of Colloidal Inorganic Nanocrystals. *Chem. Rev.* **2018**, *118* (16), 7804–7864. https://doi.org/10.1021/acs.chemrev.8b00158.
(23) Seo, D.; Park, J. C.; Song, H. Polyhedral Gold Nanocrystals with Oh Symmetry: From Octahedra to Cubes. *J. Am. Chem. Soc.* **2006**, *128* (46), 14863–14870. https://doi.org/10.1021/ja062892u.
(24) Zhou, S.; Li, J.; Gilroy, K. D.; Tao, J.; Zhu, C.; Yang, X.; Sun, X.; Xia, Y. Facile Synthesis of Silver Nanocubes with Sharp Corners and Edges in an Aqueous Solution. *ACS Nano* **2016**, *10* (11), 9861–9870. https://doi.org/10.1021/acsnano.6b05776.
(25) Sherry, L. J.; Chang, S.-H.; Schatz, G. C.; Van Duyne, R. P.; Wiley, B. J.; Xia, Y. Localized Surface Plasmon Resonance Spectroscopy of Single Silver Nanocubes. *Nano Lett.* **2005**, *5* (10), 2034–2038. https://doi.org/10.1021/nl0515753.
(26) Hoang, T. B.; Akselrod, G. M.; Argyropoulos, C.; Huang, J.; Smith, D. R.; Mikkelsen, M. H. Ultrafast Spontaneous Emission Source Using Plasmonic Nanoantennas. *Nat. Commun.* **2015**, *6*, 7788. https://doi.org/10.1038/ncomms8788.
(27) Hrelescu, C.; Sau, T. K.; Rogach, A. L.; Jäckel, F.; Feldmann, J. Single Gold Nanostars Enhance Raman Scattering. *Appl. Phys. Lett.* **2009**, *94* (15), 153113. https://doi.org/10.1063/1.3119642.
(28) Stiles, P. L.; Dieringer, J. A.; Shah, N. C.; Duyne, R. P. V. Surface-Enhanced Raman Spectroscopy. *Annu. Rev. Anal. Chem.* **2008**, *1* (1),

601–626. https://doi.org/10.1146/annurev.anchem.1.031207.112814.
(29) Jansons, A. W.; Hutchison, J. E. Continuous Growth of Metal Oxide Nanocrystals: Enhanced Control of Nanocrystal Size and Radial Dopant Distribution. *ACS Nano* **2016**, *10* (7), 6942–6951. https://doi.org/10.1021/acsnano.6b02796.
(30) Ito, D.; Yokoyama, S.; Zaikova, T.; Masuko, K.; Hutchison, J. E. Synthesis of Ligand-Stabilized Metal Oxide Nanocrystals and Epitaxial Core/Shell Nanocrystals via a Lower-Temperature Esterification Process. *ACS Nano* **2014**, *8* (1), 64–75. https://doi.org/10.1021/nn401888h.
(31) Kovalenko, M. V.; Manna, L.; Cabot, A.; Hens, Z.; Talapin, D. V.; Kagan, C. R.; Klimov, V. I.; Rogach, A. L.; Reiss, P.; Milliron, D. J.; et al. Prospects of Nanoscience with Nanocrystals. *ACS Nano* **2015**, *9* (2), 1012–1057. https://doi.org/10.1021/nn506223h.
(32) Murray, C. B.; Norris, D. J.; Bawendi, M. G. Synthesis and Characterization of Nearly Monodisperse CdE (E = Sulfur, Selenium, Tellurium) Semiconductor Nanocrystallites. *J. Am. Chem. Soc.* **1993**, *115* (19), 8706–8715. https://doi.org/10.1021/ja00072a025.
(33) Allen, P. M.; Walker, B. J.; Bawendi, M. G. Mechanistic Insights into the Formation of InP Quantum Dots. *Angew. Chem. Int. Ed.* **2010**, *49* (4), 760–762. https://doi.org/10.1002/anie.200905632.
(34) Weidman, M. C.; Beck, M. E.; Hoffman, R. S.; Prins, F.; Tisdale, W. A. Monodisperse, Air-Stable PbS Nanocrystals via Precursor Stoichiometry Control. *ACS Nano* **2014**, *8* (6), 6363–6371. https://doi.org/10.1021/nn5018654.
(35) Shen, G.; Guyot-Sionnest, P. HgS and HgS/CdS Colloidal Quantum Dots with Infrared Intraband Transitions and Emergence of a Surface Plasmon. *J. Phys. Chem. C* **2016**, *120* (21), 11744–11753. https://doi.org/10.1021/acs.jpcc.6b04014.
(36) Willets, K. A.; Van Duyne, R. P. Localized Surface Plasmon Resonance Spectroscopy and Sensing. *Annu. Rev. Phys. Chem.* **2007**, *58* (1), 267–297. https://doi.org/10.1146/annurev.physchem.58.032806.104607.
(37) Dong, A.; Jiao, Y.; Milliron, D. J. Electronically Coupled Nanocrystal Superlattice Films by in Situ Ligand Exchange at the Liquid–Air Interface. *ACS Nano* **2013**, *7* (12), 10978–10984. https://doi.org/10.1021/nn404566b.
(38) Dong, A.; Chen, J.; Oh, S. J.; Koh, W.; Xiu, F.; Ye, X.; Ko, D.-K.; Wang, K. L.; Kagan, C. R.; Murray, C. B. Multiscale Periodic Assembly of Striped Nanocrystal Superlattice Films on a Liquid Surface. *Nano Lett.* **2011**, *11* (2), 841–846. https://doi.org/10.1021/nl104208x.
(39) Winzer, P. J.; Neilson, D. T.; Chraplyvy, A. R. Fiber-Optic Transmission and Networking: The Previous 20 and the next 20 Years [Invited]. *Opt. Express* **2018**, *26* (18), 24190–24239. https://doi.org/10.1364/OE.26.024190.
(40) Keiser, G. Optical Fiber Communications. In *Wiley Encyclopedia of Telecommunications*; Wiley, 2003. https://doi.org/10.1002/0471219282.eot158.
(41) Akselrod, G. M.; Argyropoulos, C.; Hoang, T. B.; Ciracì, C.; Fang, C.; Huang, J.; Smith, D. R.; Mikkelsen, M. H. Probing the Mechanisms of Large Purcell Enhancement in Plasmonic Nanoantennas. *Nat. Photonics* **2014**, *8* (11), 835–840. https://doi.org/10.1038/nphoton.2014.228.
(42) Wu, Y.; Li, G.; Camden, J. P. Probing Nanoparticle Plasmons with Electron Energy Loss Spectroscopy. *Chem. Rev.* **2018**, *118* (6), 2994–3031. https://doi.org/10.1021/acs.chemrev.7b00354.
(43) Krivanek, O. L.; Lovejoy, T. C.; Dellby, N.; Carpenter, R. W. Monochromated STEM with a 30 MeV-Wide, Atom-Sized Electron Probe. *Microscopy* **2013**, *62* (1), 3–21. https://doi.org/10.1093/jmicro/dfs089.
(44) Spiegelberg, J.; Idrobo, J. C.; Herklotz, A.; Ward, T. Z.; Zhou, W.; Rusz, J. Local Low Rank Denoising for Enhanced Atomic Resolution Imaging. *Ultramicroscopy* **2018**, *187*, 34–42. https://doi.org/10.1016/j.ultramic.2018.01.012.
(45) Hachtel, J. A.; Huang, J.; Popovs, I.; Jansone-Popova, S.; Keum, J. K.; Jakowski, J.; Lovejoy, T. C.; Dellby, N.; Krivanek, O. L.; Idrobo, J. C. Identification of Site-Specific Isotopic Labels by Vibrational Spectroscopy in the Electron Microscope. *Science* **2019**, *363* (6426), 525–528. https://doi.org/10.1126/science.aav5845.
(46) Kim, B. H.; Staller, C. M.; Cho, S. H.; Heo, S.; Garrison, C. E.; Kim, J.; Milliron, D. J. High Mobility in Nanocrystal-Based Transparent Conducting Oxide Thin Films. *ACS Nano* **2018**, *12* (4), 3200–3208. https://doi.org/10.1021/acsnano.7b06783.
(47) Toby, B. H.; Von Dreele, R. B. GSAS-II: The Genesis of a Modern Open-Source All Purpose Crystallography Software Package. *J. Appl. Crystallogr.* **2013**, *46* (2), 544–549. https://doi.org/10.1107/S0021889813003531.
(48) Li, J.; Liu, L.; Sham, T.-K. 2D XANES–XEOL Spectroscopy Studies of Morphology-Dependent Phase Transformation and Corresponding Luminescence from Hierarchical TiO2 Nanostructures. *Chem. Mater.* **2015**, *27* (8), 3021–3029. https://doi.org/10.1021/acs.chemmater.5b00363.
(49) Pearson, R. G. Hard and Soft Acids and Bases, HSAB, Part 1: Fundamental Principles. *J. Chem. Educ.* **1968**, *45* (9), 581. https://doi.org/10.1021/ed045p581.
(50) Agrawal, A.; Cho, S. H.; Zandi, O.; Ghosh, S.; Johns, R. W.; Milliron, D. J. Localized Surface Plasmon Resonance in Semiconductor Nanocrystals. *Chem. Rev.* **2018**, *118* (6), 3121–3207. https://doi.org/10.1021/acs.chemrev.7b00613.
(51) Gordon, T. R.; Cargnello, M.; Paik, T.; Mangolini, F.; Weber, R. T.; Fornasiero, P.; Murray, C. B. Nonaqueous Synthesis of TiO2 Nanocrystals Using TiF4 to Engineer Morphology, Oxygen Vacancy Concentration, and Photocatalytic Activity. *J. Am. Chem. Soc.* **2012**, *134* (15), 6751–6761. https://doi.org/10.1021/ja300823a.
(52) Yang, H. G.; Sun, C. H.; Qiao, S. Z.; Zou, J.; Liu, G.; Smith, S. C.; Cheng, H. M.; Lu, G. Q. Anatase TiO2 Single Crystals with a Large Percentage of Reactive Facets. *Nature* **2008**, *453* (7195), 638–641. https://doi.org/10.1038/nature06964.
(53) Walsh, A.; A. Catlow, C. R. Structure, Stability and Work Functions of the Low Index Surfaces of Pure Indium Oxide and Sn-Doped Indium Oxide (ITO) from Density Functional Theory. *J. Mater. Chem.* **2010**, *20* (46), 10438–10444. https://doi.org/10.1039/C0JM01816C.
(54) Li, J.; Liu, C.; Ye, Y.; Zhu, J.; Wang, S.; Guo, J.; Sham, T.-K. Tracking the Local Effect of Fluorine Self-Doping in Anodic TiO2 Nanotubes. *J. Phys. Chem. C* **2016**, *120* (8), 4623–4628. https://doi.org/10.1021/acs.jpcc.5b11445.
(55) Karsi, N.; Lang, P.; Chehimi, M.; Delamar, M.; Horowitz, G. Modification of Indium Tin Oxide Films by Alkanethiol and Fatty Acid Self-Assembled Monolayers: A Comparative Study. *Langmuir* **2006**, *22* (7), 3118–3124. https://doi.org/10.1021/la052677b.
(56) Wang, H.; Dou, K.; Teoh, W. Y.; Zhan, Y.; Hung, T. F.; Zhang, F.; Xu, J.; Zhang, R.; Rogach, A. L. Engineering of Facets, Band Structure, and Gas-Sensing Properties of Hierarchical Sn2+-Doped SnO2 Nanostructures. *Adv. Funct. Mater.* **2013**, *23* (38), 4847–4853. https://doi.org/10.1002/adfm.201300303.
(57) Wang, H.; Rogach, A. L. Hierarchical SnO2 Nanostructures: Recent Advances in Design, Synthesis, and Applications. *Chem. Mater.* **2014**, *26* (1), 123–133. https://doi.org/10.1021/cm4018248.
(58) Frank, G.; Köstlin, H. Electrical Properties and Defect Model of Tin-Doped Indium Oxide Layers. *Appl. Phys. A* **1982**, *27* (4), 197–206. https://doi.org/10.1007/BF00619080.
(59) Comin, A.; Manna, L. New Materials for Tunable Plasmonic Colloidal Nanocrystals. *Chem. Soc. Rev.* **2014**, *43* (11), 3957–3975. https://doi.org/10.1039/C3CS60265F.
(60) Subba Ramaiah, K.; Sundara Raja, V. Structural and Electrical Properties of Fluorine Doped Tin Oxide Films Prepared by Spray-Pyrolysis Technique. *Appl. Surf. Sci.* **2006**, *253* (3), 1451–1458. https://doi.org/10.1016/j.apsusc.2006.02.019.
(61) Avadhut, Y. S.; Weber, J.; Hammarberg, E.; Feldmann, C.; Schellenberg, I.; Pöttgen, R.; Schmedt auf der Günne, J. Study on the Defect Structure of SnO2:F Nanoparticles by High-Resolution Solid-State NMR. *Chem. Mater.* **2011**, *23* (6), 1526–1538. https://doi.org/10.1021/cm103286t.
(62) Kröger, F. A.; Vink, H. J. Relations between the Concentrations of Imperfections in Crystalline Solids. In *Solid State Physics*; Seitz, F., Turnbull, D., Eds.; Academic Press, 1956; Vol. 3, pp 307–435. https://doi.org/10.1016/S0081-1947(08)60135-6.
(63) Runnerstrom, E. L.; Kelley, K. P.; Sachet, E.; Shelton, C. T.; Maria, J.-P. Epsilon-near-Zero Modes and Surface Plasmon Resonance in Fluorine-Doped Cadmium Oxide Thin Films. *ACS Photonics* **2017**, *4* (8), 1885–1892. https://doi.org/10.1021/acsphotonics.7b00429.
(64) Seo, J.-S.; Jeon, J.-H.; Hwang, Y. H.; Park, H.; Ryu, M.; Park, S.-H. K.; Bae, B.-S. Solution-Processed Flexible Fluorine-Doped Indium Zinc Oxide Thin-Film Transistors Fabricated on Plastic Film at Low Temperature. *Sci. Rep.* **2013**, *3*, srep02085. https://doi.org/10.1038/srep02085.
(65) Maruyama, T.; Nakai, T. Fluorine-doped Indium Oxide Thin Films Prepared by Chemical Vapor Deposition. *J. Appl. Phys.* **1992**, *71* (6), 2915–2917. https://doi.org/10.1063/1.351023.
(66) Shannon, R. D. Revised Effective Ionic Radii and Systematic Studies of Interatomic Distances in Halides and Chalcogenides. *Acta Crystallogr. A* **1976**, *32* (5), 751–767. https://doi.org/10.1107/S0567739476001551.
(67) Nadaud, N.; Lequeux, N.; Nanot, M.; Jové, J.; Roisnel, T. Structural Studies of Tin-Doped Indium Oxide (ITO) and In4Sn3O12. *J. Solid*

State Chem. **1998**, *135* (1), 140–148. https://doi.org/10.1006/jssc.1997.7613.
(68) Akkad, F. E.; Joseph, S. Physicochemical Characterization of Point Defects in Fluorine Doped Tin Oxide Films. *J. Appl. Phys.* **2012**, *112* (2), 023501. https://doi.org/10.1063/1.4736798.
(69) Lounis, S. D.; Runnerstrom, E. L.; Llordes, A.; Milliron, D. J. Defect Chemistry and Plasmon Physics of Colloidal Metal Oxide Nanocrystals. *J Phys Chem Lett* **2014**, *5*, 1564–1574. https://doi.org/10.1021/jz500440e.
(70) Mergel, D.; Qiao, Z. Dielectric Modelling of Optical Spectra of Thin In 2 O 3 : Sn Films. *J. Phys. Appl. Phys.* **2002**, *35* (8), 794. https://doi.org/10.1088/0022-3727/35/8/311.
(71) Hamberg, I.; Granqvist, C. G. Evaporated Sn-doped In2O3 Films: Basic Optical Properties and Applications to Energy-efficient Windows. *J. Appl. Phys.* **1986**, *60* (11), R123–R160. https://doi.org/10.1063/1.337534.
(72) Hamberg, I.; Granqvist, C. G. Optical Properties of Transparent and Heat-reflecting Indium Tin Oxide Films: The Role of Ionized Impurity Scattering. *Appl. Phys. Lett.* **1984**, *44* (8), 721–723. https://doi.org/10.1063/1.94896.
(73) Gerlach, E. Carrier Scattering and Transport in Semiconductors Treated by the Energy-Loss Method. *J. Phys. C Solid State Phys.* **1986**, *19* (24), 4585–4603. https://doi.org/10.1088/0022-3719/19/24/004.
(74) Lounis, S. D.; Runnerstrom, E. L.; Bergerud, A.; Nordlund, D.; Milliron, D. J. Influence of Dopant Distribution on the Plasmonic Properties of Indium Tin Oxide Nanocrystals. *J. Am. Chem. Soc.* **2014**, *136* (19), 7110–7116. https://doi.org/10.1021/ja502541z.
(75) Runnerstrom, E. L.; Bergerud, A.; Agrawal, A.; Johns, R. W.; Dahlman, C. J.; Singh, A.; Selbach, S. M.; Milliron, D. J. Defect Engineering in Plasmonic Metal Oxide Nanocrystals. *Nano Lett.* **2016**, *16* (5), 3390–3398. https://doi.org/10.1021/acs.nanolett.6b01171.
(76) Bel Hadj Tahar, R.; Ban, T.; Ohya, Y.; Takahashi, Y. Tin Doped Indium Oxide Thin Films: Electrical Properties. *J. Appl. Phys.* **1998**, *83* (5), 2631–2645. https://doi.org/10.1063/1.367025.
(77) Tandon, B.; Ghosh, S.; Milliron, D. J. Dopant Selection Strategy for High-Quality Factor Localized Surface Plasmon Resonance from Doped Metal Oxide Nanocrystals. *Chem. Mater.* **2019**. https://doi.org/10.1021/acs.chemmater.9b02917.
(78) Pietryga, J. M.; Park, Y.-S.; Lim, J.; Fidler, A. F.; Bae, W. K.; Brovelli, S.; Klimov, V. I. Spectroscopic and Device Aspects of Nanocrystal Quantum Dots. *Chem. Rev.* **2016**, *116* (18), 10513–10622. https://doi.org/10.1021/acs.chemrev.6b00169.
(79) Korgel, B. A.; Fullam, S.; Connolly, S.; Fitzmaurice, D. Assembly and Self-Organization of Silver Nanocrystal Superlattices: Ordered "Soft Spheres." *J. Phys. Chem. B* **1998**, *102* (43), 8379–8388. https://doi.org/10.1021/jp981598o.
(80) Hugall, J. T.; Singh, A.; van Hulst, N. F. Plasmonic Cavity Coupling. *ACS Photonics* **2018**, *5* (1), 43–53. https://doi.org/10.1021/acsphotonics.7b01139.
(81) Pelton, M. Modified Spontaneous Emission in Nanophotonic Structures. *Nat. Photonics* **2015**, *9* (7), 427–435. https://doi.org/10.1038/nphoton.2015.103.
(82) Singh, A.; de Roque, P. M.; Calbris, G.; Hugall, J. T.; van Hulst, N. F. Nanoscale Mapping and Control of Antenna-Coupling Strength for Bright Single Photon Sources. *Nano Lett.* **2018**, *18* (4), 2538–2544. https://doi.org/10.1021/acs.nanolett.8b00239.
(83) Kockum, A. F.; Miranowicz, A.; Liberato, S. D.; Savasta, S.; Nori, F. Ultrastrong Coupling between Light and Matter. *Nat. Rev. Phys.* **2019**, *1* (1), 19. https://doi.org/10.1038/s42254-018-0006-2.
(84) Vasa, P.; Lienau, C. Strong Light–Matter Interaction in Quantum Emitter/Metal Hybrid Nanostructures. *ACS Photonics* **2018**, *5* (1), 2–23. https://doi.org/10.1021/acsphotonics.7b00650.
(85) Vasa, P.; Wang, W.; Pomraenke, R.; Lammers, M.; Maiuri, M.; Manzoni, C.; Cerullo, G.; Lienau, C. Real-Time Observation of Ultrafast Rabi Oscillations between Excitons and Plasmons in Metal Nanostructures with J-Aggregates. *Nat. Photonics* **2013**, *7* (2), 128–132. https://doi.org/10.1038/nphoton.2012.340.
(86) Purcell, E. M. Spontaneous Emission Probabilities at Radio Frequencies. In *Confined Electrons and Photons: New Physics and Applications*; Burstein, E., Weisbuch, C., Eds.; NATO ASI Series; Springer US: Boston, MA, 1995; pp 839–839. https://doi.org/10.1007/978-1-4615-1963-8_40.
(87) Fox, M. *Quantum Optics: An Introduction*; Oxford University Press USA - OSO: Oxford, UNITED KINGDOM, 2006.
(88) Coccioli, R.; Boroditsky, M.; Kim, K. W.; Rahmat-Samii, Y.; Yablonovitch, E. Smallest Possible Electromagnetic Mode Volume in a Dielectric Cavity. *IEE Proc. - Optoelectron.* **1998**, *145* (6), 391–397. https://doi.org/10.1049/ip-opt:19982468.
(89) Sauvan, C.; Hugonin, J. P.; Maksymov, I. S.; Lalanne, P. Theory of the Spontaneous Optical Emission of Nanosize Photonic and Plasmon Resonators. *Phys. Rev. Lett.* **2013**, *110* (23), 237401. https://doi.org/10.1103/PhysRevLett.110.237401.
(90) Gérard, J.-M. Solid-State Cavity-Quantum Electrodynamics with Self-Assembled Quantum Dots. In *Single Quantum Dots: Fundamentals, Applications, and New Concepts*; Topics in Applied Physics; Springer Berlin Heidelberg: Berlin, Heidelberg, 2003; pp 269–314. https://doi.org/10.1007/978-3-540-39180-7_7.
(91) Chikkaraddy, R.; de Nijs, B.; Benz, F.; Barrow, S. J.; Scherman, O. A.; Rosta, E.; Demetriadou, A.; Fox, P.; Hess, O.; Baumberg, J. J. Single-Molecule Strong Coupling at Room Temperature in Plasmonic Nanocavities. *Nature* **2016**, *535* (7610), 127–130. https://doi.org/10.1038/nature17974.
(92) Kristensen, P. T.; Hughes, S. Modes and Mode Volumes of Leaky Optical Cavities and Plasmonic Nanoresonators. *ACS Photonics* **2014**, *1* (1), 2–10. https://doi.org/10.1021/ph400114e.
(93) Schmidt, F.-P.; Ditlbacher, H.; Hohenester, U.; Hohenau, A.; Hofer, F.; Krenn, J. R. Dark Plasmonic Breathing Modes in Silver Nanodisks. *Nano Lett.* **2012**, *12* (11), 5780–5783. https://doi.org/10.1021/nl3030938.
(94) Fang, W.; Xu, J. Y.; Yamilov, A.; Cao, H.; Ma, Y.; Ho, S. T.; Solomon, G. S. Large Enhancement of Spontaneous Emission Rates of InAs Quantum Dots in GaAs Microdisks. *Opt. Lett.* **2002**, *27* (11), 948–950. https://doi.org/10.1364/OL.27.000948.
(95) Maier, S. A. Plasmonic Field Enhancement and SERS in the Effective Mode Volume Picture. *Opt. Express* **2006**, *14* (5), 1957–1964. https://doi.org/10.1364/OE.14.001957.
(96) Yuen-Zhou, J.; Saikin, S. K.; Zhu, T.; Onbasli, M. C.; Ross, C. A.; Bulovic, V.; Baldo, M. A. Plexciton Dirac Points and Topological Modes. *Nat. Commun.* **2016**, *7*, 11783. https://doi.org/10.1038/ncomms11783.
(97) Aslam, U.; Rao, V. G.; Chavez, S.; Linic, S. Catalytic Conversion of Solar to Chemical Energy on Plasmonic Metal Nanostructures. *Nat. Catal.* **2018**, *1* (9), 656. https://doi.org/10.1038/s41929-018-0138-x.
(98) Zhan, C.; Chen, X.-J.; Yi, J.; Li, J.-F.; Wu, D.-Y.; Tian, Z.-Q. From Plasmon-Enhanced Molecular Spectroscopy to Plasmon-Mediated Chemical Reactions. *Nat. Rev. Chem.* **2018**, *2* (9), 216. https://doi.org/10.1038/s41570-018-0031-9.
(99) Caldwell, J. D.; Aharonovich, I.; Cassabois, G.; Edgar, J. H.; Gil, B.; Basov, D. N. Photonics with Hexagonal Boron Nitride. *Nat. Rev. Mater.* **2019**, *4* (8), 552–567. https://doi.org/10.1038/s41578-019-0124-1.
(100) Miyata, K.; Meggiolaro, D.; Trinh, M. T.; Joshi, P. P.; Mosconi, E.; Jones, S. C.; Angelis, F. D.; Zhu, X.-Y. Large Polarons in Lead Halide Perovskites. *Sci. Adv.* **2017**, *3* (8), e1701217. https://doi.org/10.1126/sciadv.1701217.
(101) Sanvitto, D.; Kéna-Cohen, S. The Road towards Polaritonic Devices. *Nat. Mater.* **2016**, *15* (10), 1061–1073. https://doi.org/10.1038/nmat4668.
(102) Ribeiro, R. F.; Martínez-Martínez, L. A.; Du, M.; Campos-Gonzalez-Angulo, J.; Yuen-Zhou, J. Polariton Chemistry: Controlling Molecular Dynamics with Optical Cavities. *Chem. Sci.* **2018**, *9* (30), 6325–6339. https://doi.org/10.1039/C8SC01043A.